Research Paper
J. Astron. Space Sci. 43(1), 1-19 (2026)
https://doi.org/10.5140/JASS.2026.43.1.1

JASS Journal of Astronomy and Space Sciences

Mapping of Patterned Regolith Textures Near the Lunar South Pole

Holly M. Brown[1†], Aaron K. Boyd[1], Mark S. Robinson[1], Megan R. Henriksen[1], Hannes Bernhardt[2]

[1]Intuitive Machines, Phoenix, AZ 85004, USA
[2]Department of Geology, University of Maryland, College Park, MD 20742, USA

Lunar slopes have distinct patterned regolith textures, but their formation mechanism remains enigmatic. We mapped the distribution of these "elephant hide" texture (EHT) occurrences in and out of shadow near the south pole (90°S to 88°S) at a scale of 1:25,000 and 1:20,000 to test if permanently shadowed regions (PSRs) have unique regolith properties relative to non-shadowed areas (polar and equatorial). We recorded the presence or absence of EHT occurrences in grid-map cells (5 and 1 km^2) using Lunar Reconnaissance Orbiter Narrow Angle Camera images of illuminated terrain, and Korea Pathfinder Lunar Orbiter ShadowCam images of permanently and temporarily shadowed terrain. We find that diffuse lighting does not interfere with the ability to identify textures. We observed that EHT has a similar likelihood to occur on shallow slopes ≤ 5° in both illuminated and permanently shadowed terrain, with no difference in texture morphology across temperature boundaries or from PSR to PSR. This suggests that regolith properties in PSRs that are relevant to EHT formation are not significantly different from those of the illuminated surface. We also observed variations of EHT across the same slopes and EHT on near-horizontal surfaces (≤ 3°) within ~500 m of the foot of slopes. This suggests that patterned regolith textures are formed by down-slope transport of loose regolith, likely driven by both episodic and continuous disturbances.

Keywords: "elephant hide" texture, permanently shadowed region, ShadowCam, Danuri, Korea Pathfinder Lunar Orbiter (KPLO), Lunar Reconnaissance Orbiter (LRO)

1. INTRODUCTION

Distinct regions of patterned regolith textures are typical of lunar slopes. This texture was characterized during the Ranger, Lunar Orbiter, and Apollo programs as a hummocky "grid patterned" ground—or "tree bark" texture—consisting of disconnected ridges and troughs forming lineaments of varying lengths (Fig. 1; Kuiper 1965; Shoemaker 1966; Crittenden 1967; Greeley 1971; Mattingly et al. 1972; Scott et al. 1972; Swann et al. 1972). High-resolution orbital data from Apollo missions 11–17, acquired with large incidence angles, revealed that the patterned texture varied on both sloped and flat surfaces (Schaber & Swann 1971; Parker et al. 1973). The direction of illumination further influenced the appearance of the lineaments: depending on lighting, they appeared either parallel to the slope or at approximately 30° to 50° to the slope (Howard & Larsen 1972; Mattingly et al. 1972; Parker et al. 1973), producing a cross-hatched pattern of discontinuous, rounded to subangular rhomboid shapes. To explain these observations, the leading hypothesis among Apollo scientists was that the patterned surface texture resulted from downslope movement of loose regolith triggered by impacts and periodic seismic shaking, especially in areas where pre-existing bedrock fractures were present (Swann et al. 1972).

Post-Apollo era studies, using high-resolution images, identified this patterned surface texture, now known as "elephant hide" texture (EHT), on both the Moon and Mercury (Plescia & Robinson 2010; Melosh 2011; Zharkova et al. 2020; Kreslavsky et al. 2021). EHT is found lunar-wide, including within mare and highland terrains, on young Copernican surfaces (Shoemaker 1966; Greeley 1971; Plescia

Received 04 OCT 2025 **Revised** 09 DEC 2025 **Accepted** 15 DEC 2025
[†]**Corresponding Author**
Tel: +1-480-330-7819, E-mail: hbrown@intuitivemachines.com
ORCID: https://orcid.org/0000-0001-9329-8464

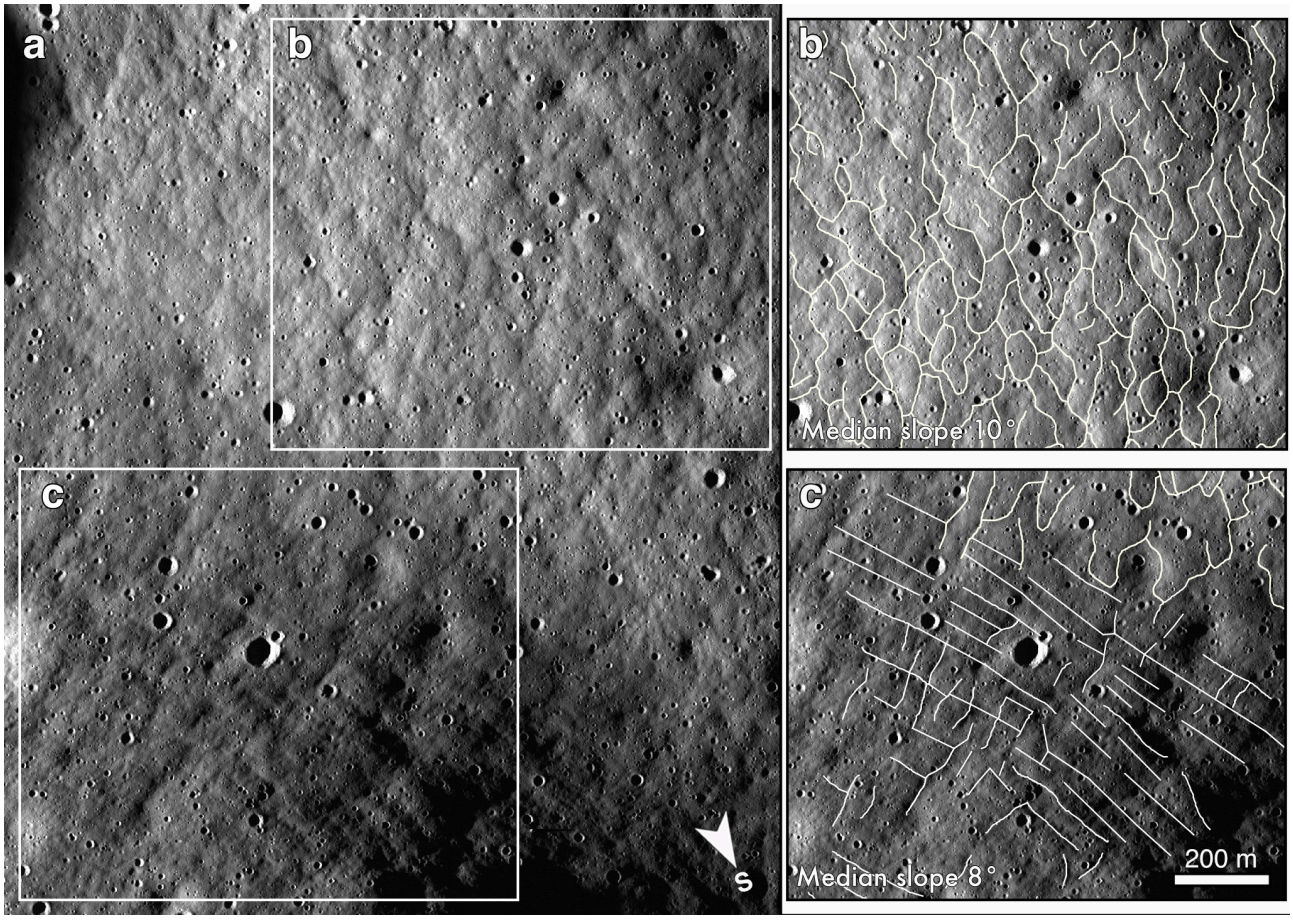

Fig. 1. Common patterned regolith textures on sloped lunar surfaces. The basemap is the Lunar Reconnaissance Orbiter Camera Narrow Angle Camera (LROC NAC) 1-meter/pixel south pole mosaic (subsolar azimuth 265°). (a) Degraded crater inner wall located just below the slope shoulder (–88.061°S, 328.347°E), with median slopes ranging from 8° to 10°. (b) "Elephant hide" texture (EHT), characterized by decameter- to ~100 meter-wide hummocky, lobate segments (white polygons; Table 1). (c) A variation of EHT, consisting of decameter-scale disconnected ridges and troughs forming lineaments of varying lengths (white lines). Surficial lineaments occur parallel to the slope or at a 30° to 50° cross-slope angle and commonly blanket lobate segments of EHT. Together, these features create a cross-hatched pattern of continuous to discontinuous rounded rhomboid shapes (shown as intersecting white lines in (c)).

& Robinson 2010; Lena & Fitzgerald 2014; Robinson et al. 2016; Kreslavsky et al. 2021; Bernhardt et al. 2022; Bondarenko et al. 2022) and inside permanently shadowed regions (PSRs) (Brown et al. 2024; Basilevsky et al. 2024; Williams et al. 2024). It has been further characterized by decameter- to ~100 meter-wide lobate segments (Fig. 1), which most commonly contour slopes 5° to 30° (Xiao et al. 2013; Kreslavsky et al. 2021; Bondarenko et al. 2022; Bondarenko 2023). However, EHT distribution is non-uniform, indicating that slope alone does not control its formation (Williams et al. 2024).

Periodic seismic shaking may explain why EHT persists on near-horizontal and concave surfaces, despite regolith gardening that would otherwise erase these small-scale features and smooth the topography over time (Ross 1968; Soderblom 1970; Antonenko 2012; Fassett & Thomson 2014; Zharkova et al. 2020; Kreslavsky et al. 2021). Nevertheless, the possible association between EHT and young tectonic features—such as whether EHT is enhanced, suppressed, or otherwise influenced near such tectonic activity—has yet to be investigated globally (Watters et al. 2015, 2019, 2024). Diurnal thermal cycling (Melosh 2011) and electrostatic dust levitation (Gold & Williams 1973) have been proposed as periodic EHT-forming processes that may contribute to regolith deposition over geologic timescales; however, these hypotheses remain a gap in the literature.

In terrestrial geomorphology, it is well understood how surface shape, slope position, regolith thickness, density, and rates of weathering influence granular material transport and deposition across the landscape (Culling 1960; Pelletier 2008; Anderson & Anderson 2010). However, how these factors contribute to forming small-scale features on airless bodies remains poorly understood. Previous workers have shown that terrestrial morphometric variables, such as curvature (surface shape) and catchment area (flow paths), generated

from high-resolution terrain models aid in interpreting the lunar landscape (Mitusov et al. 2023); however, these techniques have yet to be applied to analyze EHT-bearing surfaces. Bondarenko (2023) generated a high-resolution terrain model using shape-from-shading techniques (Bondarenko et al. 2018) and Lunar Reconnaissance Orbiter Camera Narrow Angle Camera (LROC NAC; Robinson et al. 2010) images to map craters on an EHT-bearing surface. They observed a lack of craters 5 to 8 m in diameter, indicating that these craters may be regolith-filled (Bondarenko 2023). Given the estimated crater depths in that size range, it was hypothesized that EHT must be mobile up to a depth of 1 m (Bondarenko 2023). However, more mapping and analysis are needed of EHT-bearing surfaces globally to constrain these depth estimates.

Recent work investigated EHT occurrence in PSRs and how diffuse secondary lighting affects the interpretation of these small-scale surface features (Basilevsky et al. 2024; Williams et al. 2024; Brown et al. 2025). In images acquired under primary illumination, each pixel has one light source. However, under diffuse secondary lighting, each pixel receives illumination from multiple sources and angles (Haruyama et al. 2008; Brown et al. 2022; Mahanti et al. 2022, 2023, 2024; Robinson et al. 2023; Martin et al. 2024). In this work, we seek to understand better how our interpretation of EHT differs under varying lighting conditions by mapping EHT in and out of shadow near the south pole (90°S to 88°S; Fig. 2) under direct illumination with LROC NAC images and comparing results to co-located ShadowCam images (Robinson et al. 2023) of the same regions while temporarily shadowed. This direct vs. secondary illumination comparison guides our interpretation of landforms in PSRs.

We search for the presence or absence of EHT using a grid-mapping technique (Voelker et al. 2017) with cells of both 5 km by 5 km and 1 km by 1 km over a fixed geographic area. Our goal is to identify the locations of EHT occurrences and compare their morphology, including specific morphometric variables (slope angle, curvature, and slope position) with those in non-shadowed polar areas to test whether PSRs show unique regolith properties. Given the globally distributed occurrence of EHT, a classification of EHT is necessary to determine the physical properties that affect its formation, which is useful for informing aspects of future landed polar exploration, such as hazard avoidance and regolith stability.

2. DATA AND METHODS

We used the US Geological Survey (USGS) 1-meter/pixel

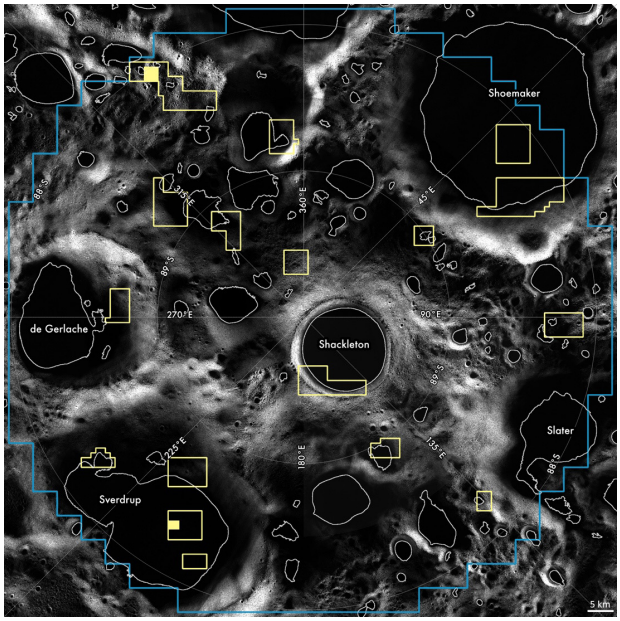

Fig. 2. Map area near the south pole (90°S to 88°S). The background is the US Geological Survey (USGS) 1-meter/pixel Lunar Reconnaissance Orbiter Camera Narrow Angle Camera (LROC NAC) average pixel value mosaic (Archinal et al. 2023). Areas within the blue boundary were mapped with 5 km by 5 km cells at 1:25,000; areas within the yellow boundaries were mapped with 1 km by 1 km cells at 1:20,000; and the areas highlighted in yellow were mapped at 1:5,000. Permanently shadowed regions are outlined in white (Mazarico et al. 2011). Data from Archinal et al. (2023), Mazarico et al. (2011).

LROC NAC controlled south pole average pixel value and subsolar longitude (time of day) mosaics (84°S to 90°S) to map EHT in illuminated terrain (Archinal et al. 2023). All images in the mosaics were aligned to the Lunar Orbiter Laser Altimeter (LOLA) reference frame using the ISIS jigsaw tool (Edmundson et al. 2012). USGS-controlled mosaic products can be downloaded from the LROC PDS archive (https://pds.lroc.im-ldi.com/data/LRO-L-LROC-5-RDR). Because lighting geometry affects the appearance of EHT (Schaber & Swann 1971; Kreslavsky et al. 2021; Bondarenko 2023; Brown et al. 2024) we primarily mapped EHT from the subsolar longitude mosaics (using images grouped in 10° bins of subsolar azimuth). The average mosaic is a composite of images from multiple lighting directions and was thus useful for identifying regions with any illumination.

For permanently shadowed terrain, which made up more than half of the map area, we selected uncontrolled ShadowCam images acquired at various times during the south pole summer. To understand the effect of diffuse secondary lighting on identification of regolith textures, we also included ShadowCam images of temporarily shadowed terrain for comparison with co-located NACs (Fig. 3; Supplementary Table S1). The ShadowCam images of temporarily shadowed terrain had 34% areal overlap with

illuminated NACs, providing suitable lighting conditions to interpret the same terrains in both datasets. All ShadowCam images were map-projected in polar stereographic projection with a pixel scale of 2 m. We did not correct image-to-image offsets (up to 50 m; Wagner et al. 2024), as the scale of the offsets did not affect our mapping in the 5 km by 5 km or 1 km by 1 km cells.

In addition to mapping EHT with LROC NAC and ShadowCam images, we measured regional morphology using the LOLA south polar 20-meter/pixel digital elevation model (LDEM; Mazarico et al. 2011; Barker et al. 2021). We computed slope and curvature using the GDAL "gdaldem" tools (GDAL/OGR contributors 2025) and the SAGA "Morphometric features" tool (Conrad et al. 2015), using their default algorithms: Horn (1981) for slope and Zevenbergen & Thorne (1987) for curvature. Horn is sensitive to short-range variation and effective over ~2 pixels (40 m), while Zevenbergen & Thorne produces smoother derivatives across ~3 pixels (60 m), making it more suitable for curvature estimation (Horn 1981; Zevenbergen & Thorne 1987; Kienzle 2004). Last, we used regional geologic (Fortezzo et al. 2020) and polar illumination (Mazarico et al. 2011) maps to compare EHT to geologic terrains and overlap with PSR extents.

2.1 Mapping Technique

We divided our study area (90°S to 88°S; 12,750 km^2) into 510 grid cells (5 km by 5 km) using the QGIS 'Create grid' algorithm (QGIS Development Team 2025). We chose a coarse map scale (1:25,000) and grid-mapping cell size that still allowed us to identify EHT lobate segments ≥ 10 meters-wide and cover a significant map area. We used a finer map scale (1:20,000; 1 km by 1 km cells) across PSR to non-PSR temperature boundaries and areas of interest (Fig. 2; Section 3.3) to investigate potential segment width variations correlated with temperature and slope morphometry. Temperature boundary regions of interest were chosen based on annual maximum temperatures using the Diviner maximum surface temperature maps (240 m/pixel; Williams et al. 2019) for reference. We chose areas where the maximum temperature difference between PSRs to non-PSRs differed by 90 K to 200 K. The temperature transition zones that we selected spanned two to six km along PSR boundaries. We also consulted the LOLA south polar PSR map (Mazarico et al. 2011) to ensure that all selected areas were within three km from a PSR boundary. Areas of interest for morphometric analysis were picked from the 5 km by 5 km grid-map observations in areas where EHT occurred on various landscape curvatures in PSRs and non-PSRs. To ensure we sampled a wide variety of slopes for the 1 km by 1 km map, we took the median slope in each cell, sorted them into 10° slope bins, and evenly sampled from those bins. In total, we mapped 709 km^2 with the 1 km by 1 km cells (352 PSR and 357 non-PSR cells, respectively).

We recorded and classified the presence or absence of

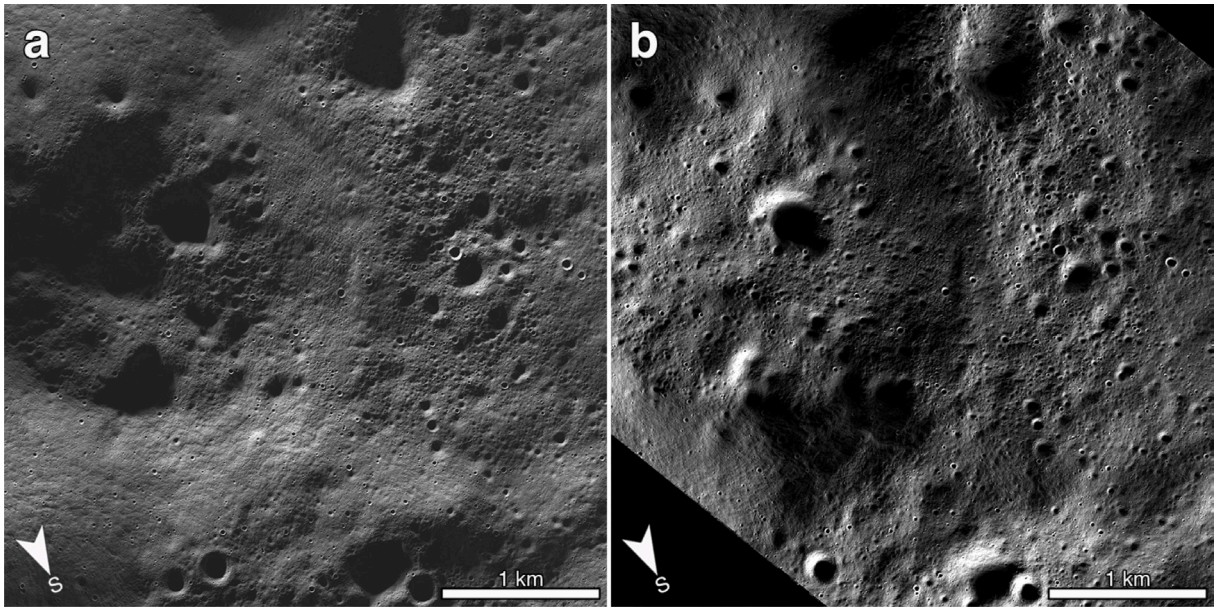

Fig. 3. Lunar Reconnaissance Orbiter Camera Narrow Angle Camera (LROC NAC) and KPLO ShadowCam observations of the same geographical extent (–89.396°S, 332.017°E) under primary (a) and diffuse secondary lighting (b). Extent is 5 km by 5 km. (a) US Geological Survey (USGS) NAC controlled 1-meter/pixel subsolar longitude mosaic with subsolar azimuth at 5°. (b) Uncontrolled ShadowCam image (M044599808S; 2-meter/pixel) taken during the south polar summer (2024-01-03).

EHT in each cell following the work in Voelker et al. (2017). EHT was classified as dominant (covering 50% to 100% of the cell), present (covering 25% to 50% of the cell), or absent (0% of the cell; Fig. 4). EHT occurrences covering 1% to 25% of the cell were classified as having mixed morphology (Table 1). For cells containing ≥ 25% EHT, we characterized morphology based on variations of texture. These variations typically corresponded with EHT segment width, shape, and size (Figs. 5 and 6; Table 1; Section 3.2). To ensure consistent interpretation of textures during grid-mapping, mapping was conducted by one person who drew on prior experience digitizing EHT segments (Brown et al. 2024). EHT segment widths were manually measured using QGIS tools and/or visually compared to the polygonal grid cells as a scale reference. The same person then re-evaluated the grid-mapping units to ensure quality and accuracy in the results.

2.2 Statistical Analysis

We used the 'Zonal Statistics' tool in QGIS to extract values for slope, curvature, and annual maximum surface temperature for each cell. Grid-mapped data (5 km by 5 km and 1 km by 1 km) were grouped as PSR, non-PSR, or a PSR boundary. We performed N-way analysis of variance (ANOVA; Sthle & Wold 1990; The Mathworks Inc. 2022) to test if a given variable in a cell (curvature and median slope) varied significantly ($p < 0.05$) among morphologic units in PSRs and non-PSRs. We performed an additional ANOVA of 1 km by 1 km cells across PSR to non-PSR boundaries to investigate the effect of temperature changes on segment width. Additionally, we tested how frequently each texture unit occurred at a given slope using all of our 1 km by 1 km cells.

Lastly, we digitized and measured lobate EHT segments in two local areas, Sverdrup crater floor (–88.332°S, 211.907°E; Fig. 7 and Supplementary Table S2) and an unnamed illuminated area near -88.047°S, 327.892°E (Fig. 1), to (1) study how EHT morphology, or segment width, changes with respect to hillslope shape, position on hillslope, and slope gradient, and (2) derive and estimate the scale of EHT-associated topography. Our grid-mapping results of EHT locations informed our decision to target these locations for detailed morphometric analysis. In addition, we chose the

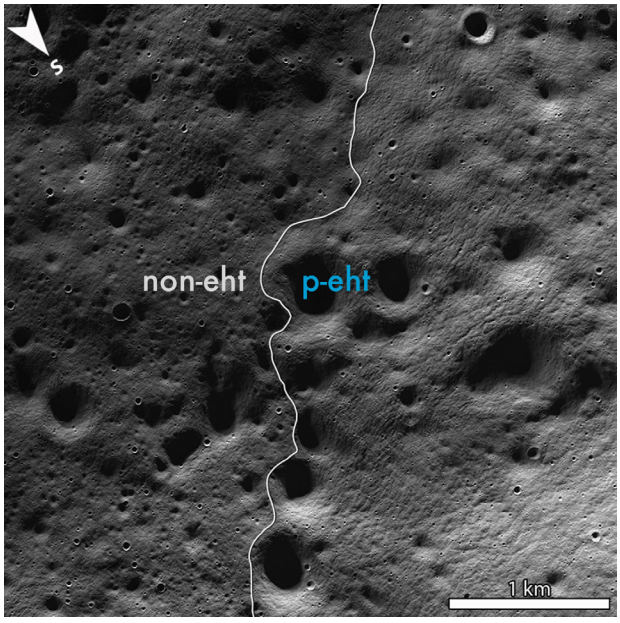

Fig. 4. Contact between prominent "elephant hide" texture (unit p-eht; Section 3.2) and a non-"elephant hide" texture (EHT) surface within a 5 km by 5 km cell (–89.61°S, 348.01°E). This cell is classified as EHT present (covering half of the cell) using the US Geological Survey (USGS) 1-meter/pixel Lunar Reconnaissance Orbiter Camera Narrow Angle Camera (LROC NAC) average pixel value mosaic (shown here) and subsolar longitude mosaics (azimuths 295° to 15°).

Table 1. Regolith textures observed at 1:25,000 within a 5 km by 5 km cell

Label	Texture name	Area (km^2)	Description	Example location (Fig. 6)
p-eht	Prominent elephant hide texture	594–2,750	Decameter- to ~100 meter-wide hummocky "prominent" lobate to sinuous segments that are separated by meters-wide troughs and most commonly contour median slopes 5° to 15°, and less commonly appear on flat surfaces. Lineaments of varying lengths commonly cross p-eht, appearing either parallel to the slope or at a 30° to 50° cross-slope angle (depending on the lighting direction), creating a cross-hatch pattern of discontinuous rounded rhomboid shapes.	–89.293°S, 315.575°E; –88.357°S, 336.492°E
m-eht	Moderate elephant hide texture	627–1,925	~100- to 250-meter-wide patterns that form "moderate" or subdued lobate segments that are separated by meter- to decameter-wide troughs and contour median slopes up to 20°. Textures gradually become less pronounced as segment size increases in width (short axis). Lineaments are less distinct.	–88.915°S, 88.555°E
ss-eht	Stair-stepped elephant hide texture	1,034–2,675	Meter- to decameter-wide wavy to linear terraced segments that are separated by meter-wide benches on median slopes 15° to 35°. Wavy ss-eht resembles p-eht where terraced segments are discontinuous. Lineaments of varying lengths commonly cross ss-eht, typically appearing perpendicular to the slope.	–88.037°S, 196.547°E
non-eht	No observable elephant hide texture	325	Cratered highlands surface or smooth crater floors with no observable EHT. Median slopes ≤ 5°.	–88.162°S, 114.476°E
mixed	Mixture of textures	5,075–10,170	Unit ss-eht mixed with m-eht, p-eht, and/or non-eht.	–88.238°S, 331.477°E

We calculated the areal coverage of textures by counting the number of cells where the texture was classified as dominant (covering most of the cell), present (covering less than half of the cell), or absent. To estimate the low end of areal coverage, we counted all dominant cells plus half the number of present cells. To calculate the upper limit, we counted both dominant and present cells as fully contributing to the areal coverage.

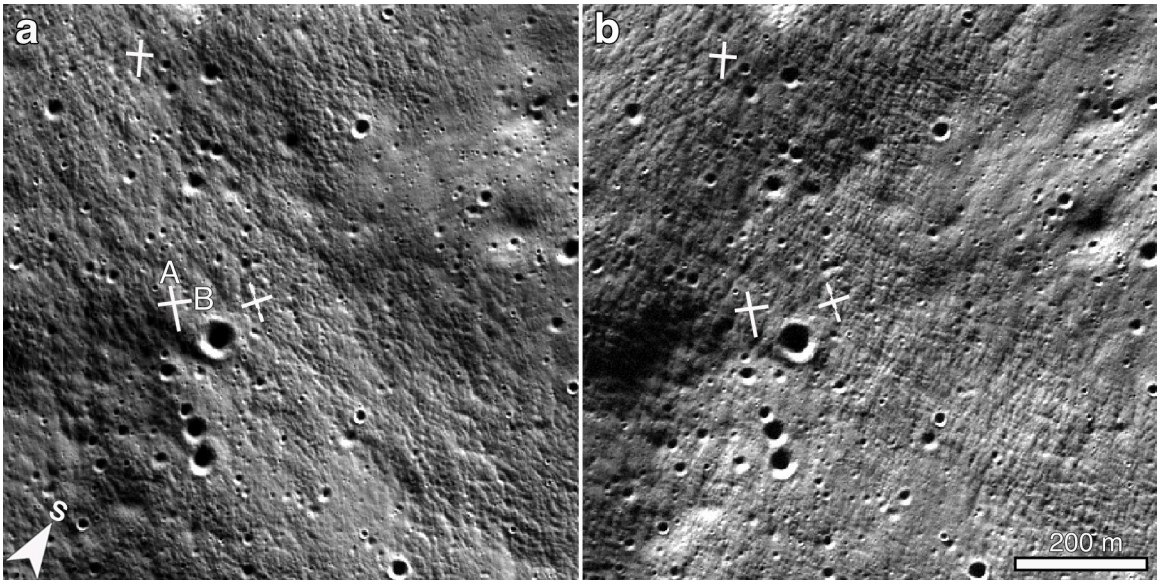

Fig. 5. The same scene on Sverdrup crater floor (–88.332°S, 211.907°E) under different secondary lighting conditions. White crosses show examples of lobate "elephant hide" texture (EHT) segments that have consistent orientation in both images and are thus suitable for measurement. Crosshairs denote the length (long axis; A) and width (short axis; B) of an EHT segment; segments shown here are ~35 meters-wide. (a) ShadowCam image (M0170132065) with secondary light coming from the east. (b) ShadowCam image (M073688240S) with secondary light coming from the northwest.

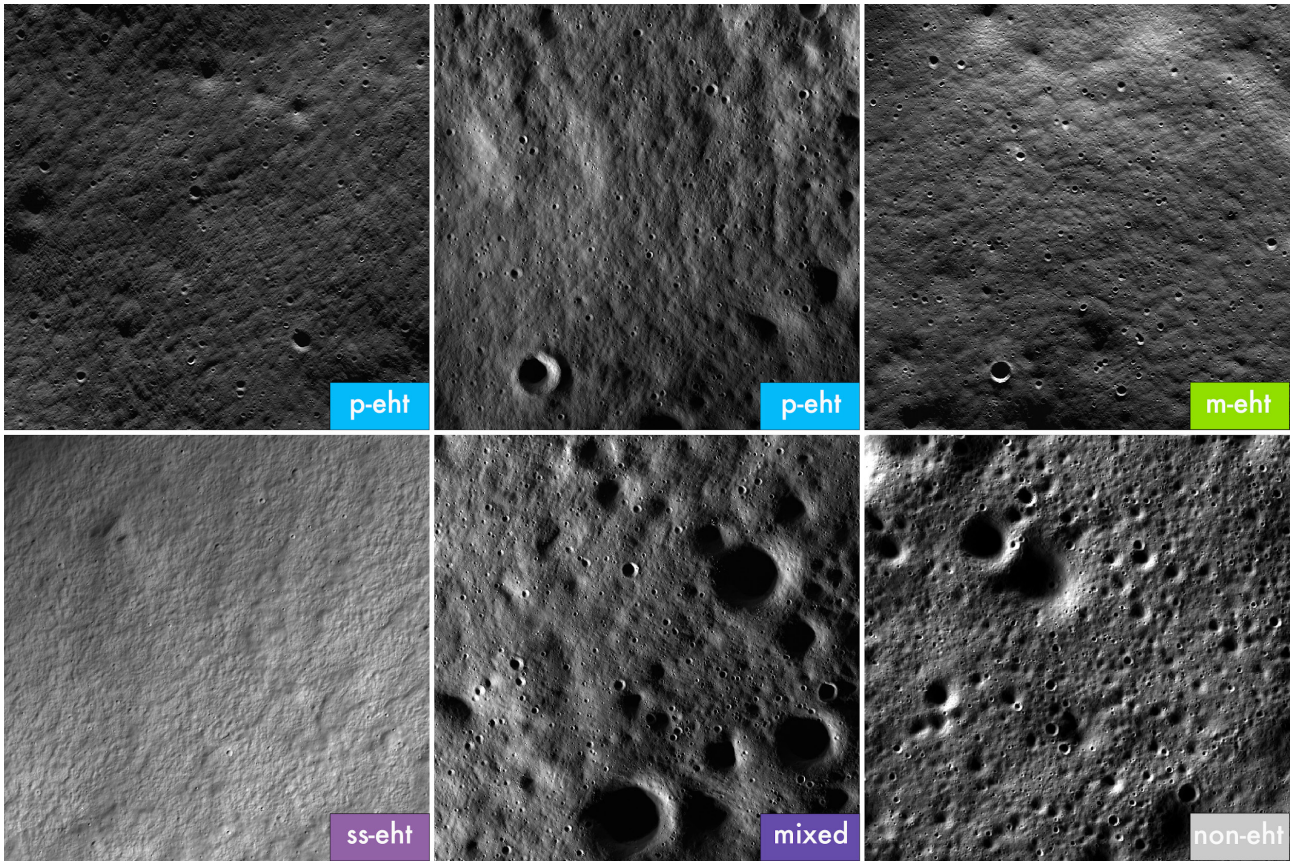

Fig. 6. Regolith textures characterized within the map area. Two variations of unit p-eht are shown: (left) a cross-hatched pattern (Fig. 1(c)) and (right) a hummocky pattern with lobate segments. Examples are 1.5 km by 1.5 km crops at 1:20,000 of the US Geological Survey (USGS) 1-meter/pixel Lunar Reconnaissance Orbiter Camera Narrow Angle Camera (LROC NAC) mosaics at varying subsolar azimuths and one ShadowCam image (labelled "non-eht"); see Table 1 for coordinates.

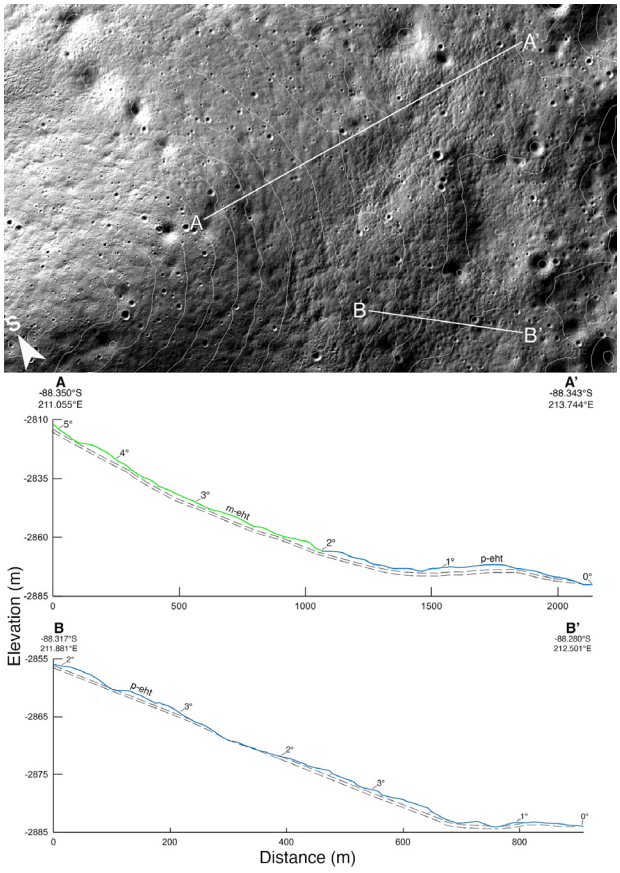

Fig. 7. Mound on the floor of Sverdrup crater showing "elephant hide" texture (EHT) morphology (ShadowCam orthophoto M016822289S and image M017013206S). The topographic profiles (A to A′ and B to B′) are taken across a 6-meter/pixel ShadowCam DEM and the 1 km by 1 km grid-map geomorphic units. The cross sections show how the geomorphic units moderate (m-eht; green) and prominent (p-eht; blue) vary with distance from the hillcrest. We estimate that the mobile segments of EHT are 0.5-meter in height; however, this estimate is subject to 1 to 2 m of uncertainty (see Section 3.4.1). The double-dashed line indicates a hypothesized gradational contact with the upper regolith layer. However, this contact may not represent the whole extent of the deformable EHT-layer. Profiles A to A′ and B to B′ are vertically exaggerated 9.4× and 10×, respectively, to show the EHT-associated topography on shallow slopes. Placements of median slope labels (°) are approximate.

mound on the floor of Sverdrup due to overlap with a high-resolution 6-meter/pixel ShadowCam DEM (Manheim et al. 2024), which allowed for rough estimates of EHT height. Since the direction of illumination can alter the perceived orientation of EHT segments (Fig. 5(a) and (b)), we used subsolar longitude mosaics with subsolar azimuths at 255° to 305° for the illuminated site and six ShadowCam images that varied by season (December to February) and sun direction (east and west) for the Sverdrup PSR. We only used EHT segment measurements that were consistent across multiple lighting directions. In total, we mapped ~4 square km at a 1:5,000 scale across both sites.

3. RESULTS

3.1 Interpreting Regolith in Shadow

We find that diffuse lighting does not affect our ability to identify EHT. For example, on both sloped and flat surfaces, we identified EHT morphology in all of the co-located NAC (illuminated) and ShadowCam (temporarily shadowed) images using the 5 km by 5 km and 1 km by 1 km cells (127 and 178 cells, respectively). We only mapped different geomorphic units at ~3% of co-locations, which were near PSR boundaries. At these co-locations, we mapped prominent EHT (p-eht) in ShadowCam images vs. moderate EHT (m-eht) in NAC images. This may be due to poor lighting at the shadow edge in NAC images. For the co-located images where we identified the same texture, EHT typically varied in appearance due to perceived orientation (Fig. 5). Unit m-eht was sometimes easier to identify in ShadowCam images.

3.2 Morphologic Unit Descriptions and Interpretations

Within our map area (5 km by 5 km cells), five morphologic units were identified (Table 1; Figs. 6 and 8): three types of EHT that we differentiated by segment width and intensity (prominent vs. moderate), surfaces completely devoid of EHT, and mixed EHT morphology within a cell (EHT and non-EHT). Contacts between EHT units are gradational and contacts between EHT and non-EHT are distinct. When we compared EHT across multiple sun azimuths, we found that the segment width (short axis) of all EHT units parallels the down-slope direction. Lineaments of varying lengths commonly cross EHT units and appear perpendicular to the slope (Fig. 5). Cells with a mixture of EHT and non-EHT are the most extensive unit, covering 43.5% of the map area.

3.2.1 Prominent Elephant Hide Texture (p-eht)

Prominent hummocky patterned regolith texture composed of decameter- to ~100 meter-wide lobate to sinuous segments separated by meters-wide troughs. Unit p-eht is observed on moderately gentle to steep talus slopes (5° to 15°), where transport is dominant, and on convex, concave, and (less commonly) flat-lying surfaces at the base of these slopes, where deposited material accumulates (Figs. 9 and 10). This texture is blanketed by meter-wide surficial lineaments of varying lengths that typically appear perpendicular to the slope (depending on the lighting direction) that together create a cross-hatched pattern of discontinuous, rounded rhomboid shapes (Figs. 1 and

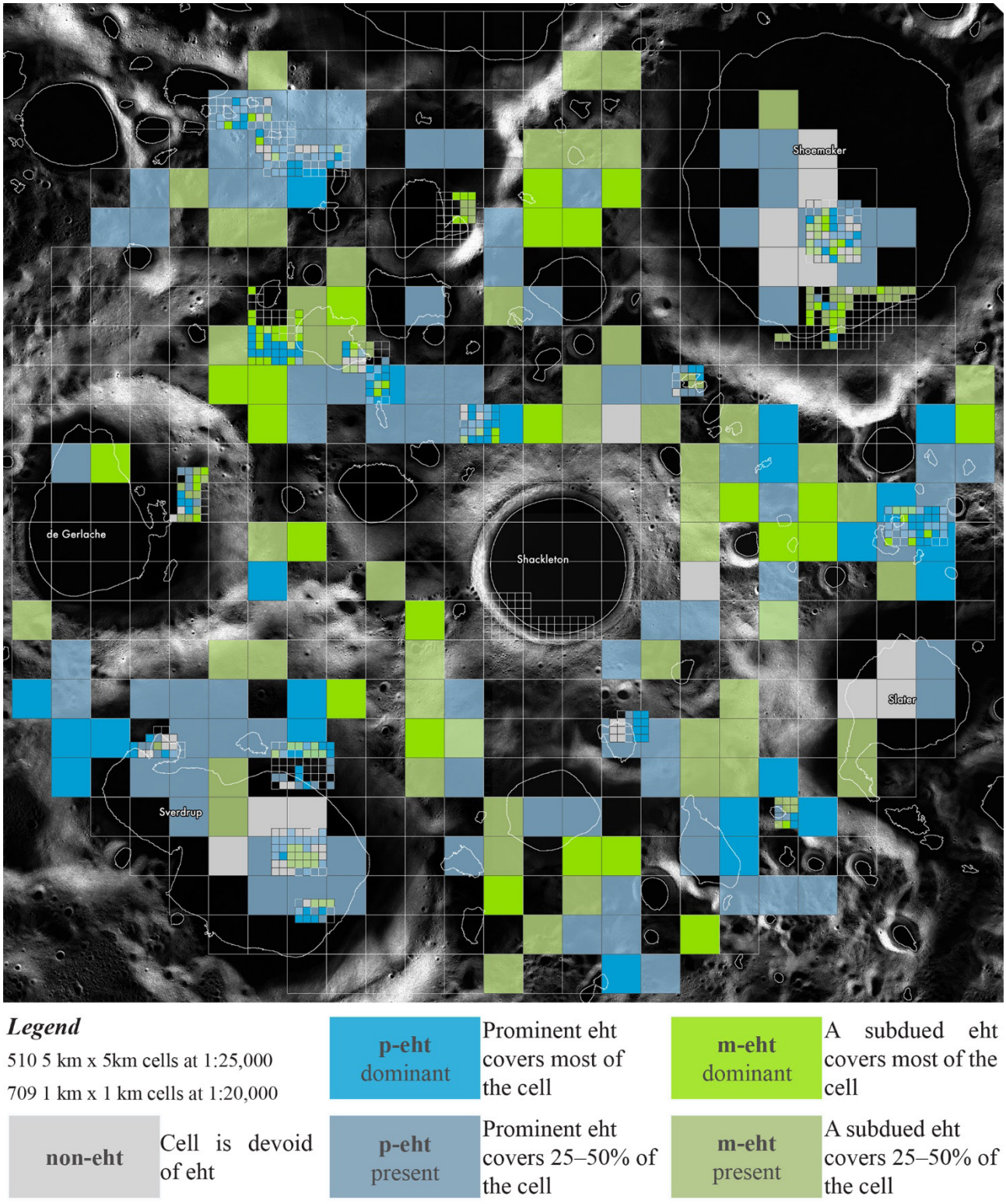

Fig. 8. "Elephant hide" texture (EHT) locations near the south pole (90° to 88°S) within 5 km by 5 km cells and regions of interest within 1 km by 1 km cells. Blue and green cells are variations of EHT, and gray is devoid of EHT. Color shading indicates texture dominance (opaque) or presence (translucent). Transparent cells are mapped as either a stair-step variation of EHT that is most common on steep slopes or a mixture of textures. Permanently shadowed region (PSR) boundaries are outlined in white.

6). Textures are most pronounced on the talus and toe of slopes, regardless of vertical or horizontal curvature in the landscape (Fig. 10).

3.2.2 Moderate Elephant Hide Texture (m-eht)

A less pronounced or subdued version of p-eht, with ~100- to 250- meter-wide lobate segments separated by meter- to decameter-wide troughs that most commonly contour median slopes up to 20° (Fig. 9). The hummocky texture gradually becomes less pronounced as segment size increases in width (short axis). Cross-hatched patterns typical of p-eht are commonly absent. Unit m-eht typically occurs on convex surfaces along and cross-contour, and on broadly-sloping pediments of gentle hillslopes ≤ 10° (Fig. 7).

3.2.3 Stair-Step Elephant Hide Texture (ss-eht)

A variation of EHT that forms a stair-stepped pattern, with meter- to decameter-wide wavy to linear segments that are separated by meter- to decameter-wide benches on median slopes 15° to 35° (Fig. 9). Wavy meter-scale ss-eht resembles p-eht with discontinuous terraced segments. Lineaments of varying lengths commonly cross ss-eht, typically appearing perpendicular to the slope. On median slopes 20° to 35°, we commonly see p-eht interspersed with stair-step textures. Unit ss-eht most commonly occurs on inner crater walls, or on steep-sloped surfaces where regolith is thinned.

3.2.4 Surfaces Devoid of Elephant Hide Texture (non-eht)

Cratered highlands surface or smooth crater floors with no observable EHT. Occurs on flat-lying to near-flat-lying areas

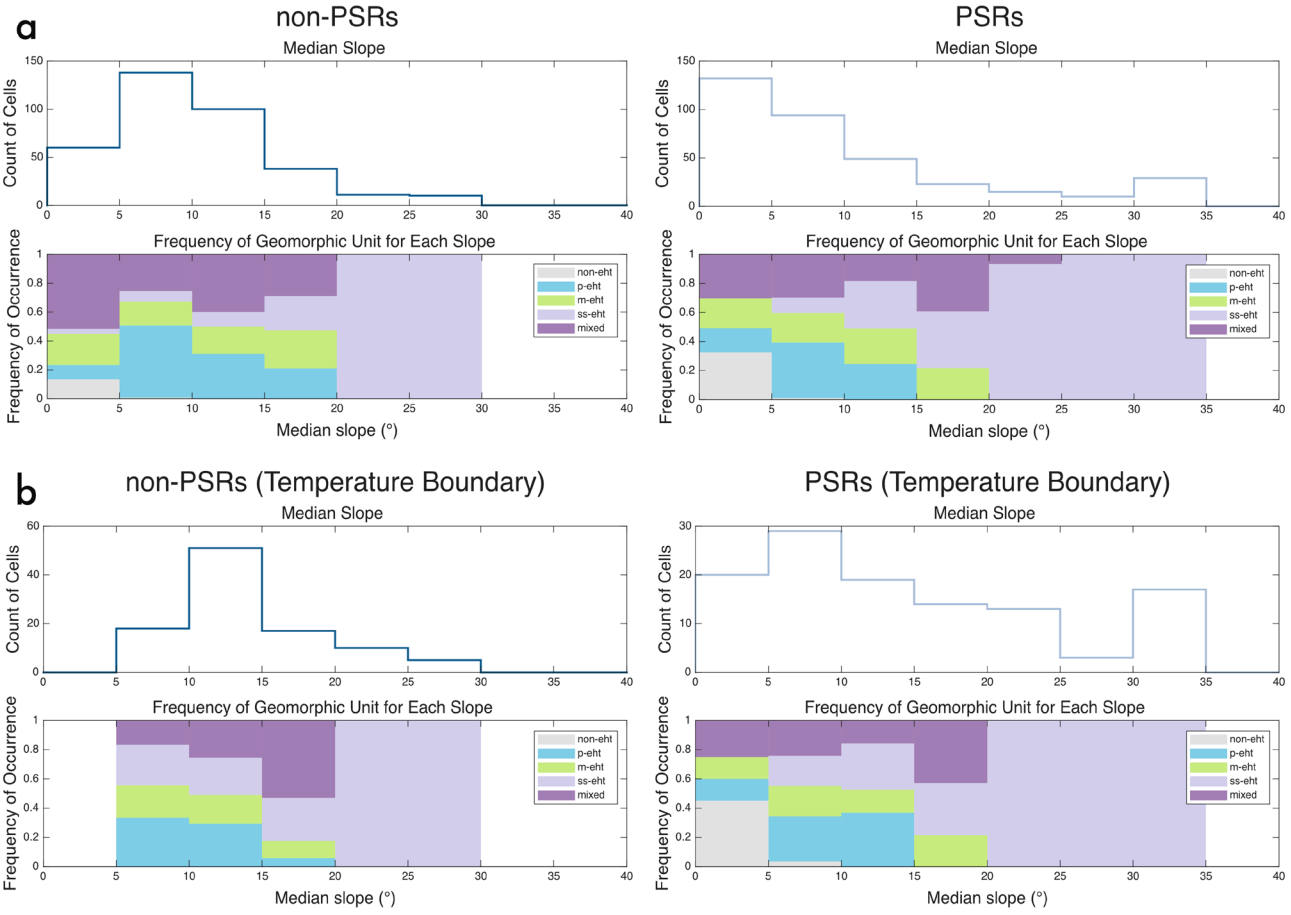

Fig. 9. Median slopes where "elephant hide" textures (EHTs; p-eht, m-eht, ss-eht) are most likely to be present or absent (unit non-eht) in permanently shadowed regions (PSRs) and non-PSRs. (a) Regions of interest mapped with 1 km by 1 km cells (1:20,000) identified using our 5 km by 5 km grid-map (Fig. 8). (b) A subset of the 1 km by 1 km cells in plot (a) mapped across PSR to non-PSR temperature boundaries (90° to 200° change in temperature; Fig. 2; Section 2.1). EHT units have a similar likelihood to occur on a given slope across polar terrains and PSR to non-PSR boundaries (up to 10% frequency difference). This indicates that variations in segment width (p-eht vs. m-eht) are not correlated with temperature changes. Our count of cells with median slopes ≤ 5° is limited by the terrain in our map area (large permanently shadowed crater floors); surfaces devoid of EHT have a similar likelihood to occur in both PSRs and non-PSRs.

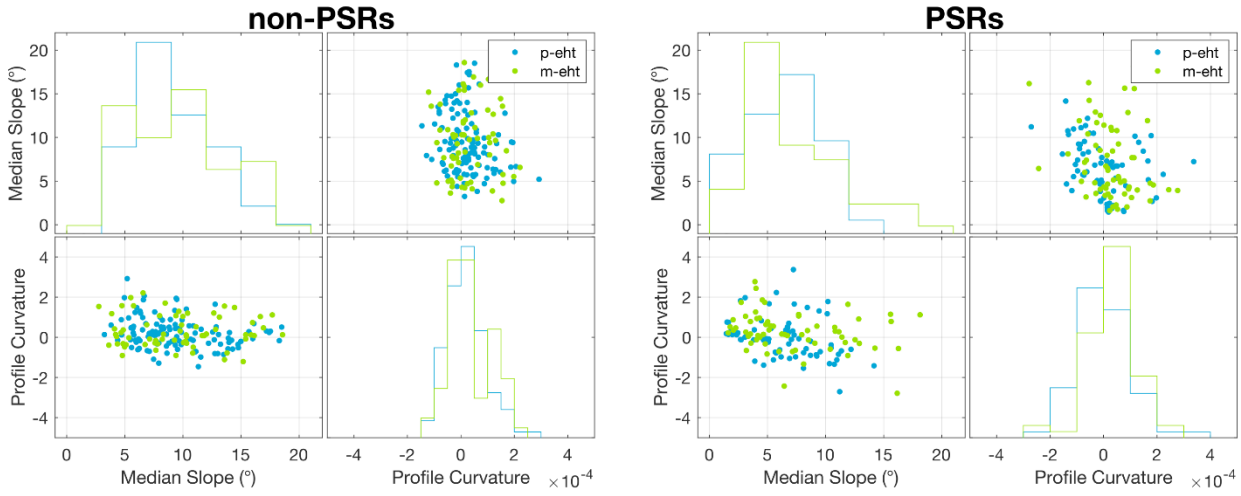

Fig. 10. Variations in "elephant hide" texture (EHT) morphology (units p-eht and m-eht) with respect to hillslope shape and slope in permanently shadowed regions (PSRs) and non-PSRs. Profile curvature measures the surface shape in the direction of maximum slope and indicates whether a surface is convex (> 0), concave (< 0), or flat/linear (= 0) in profile, as defined by Wood (1996, 2009) and Conrad et al. (2015). Both units occur across varying hill shapes and slopes, unit m-eht (a moderate or subdued EHT) is more likely to occur on convex surfaces than unit p-eht. Data from Wood (1996, 2009), Conrad et al. (2015).

(≤ 5°; Fig. 9) past the toe of a slope. Unit non-eht displays sharp contacts with p-eht and ss-eht.

3.2.5 Mixed (ss-eht, p-eht, m-eht, and non-eht)

Unit ss-eht mixed with m-eht, p-eht, and/or non-eht. We mapped this unit when no dominant texture was discernible within a cell.

3.2.6 Interpretation (units p-eht, m-eht, and ss-eht)

When comparing morphologies at 1:20:000 (1 km by 1 km) scale (Fig. 9), we found that both the landscape shape (curvature along and across contour lines) and slope position (distance from hillcrest) affect EHT morphology. Because unit m-eht is the most common morphology on convex surfaces at different positions along hillslopes, we interpret this unit to be regolith that diverged laterally downslope to create longer, or more subdued, EHT segments. In contrast, the higher-intensity EHT (p-eht) and associated cross-hatched pattern (Crittenden 1967; Greeley 1971; Mattingly et al. 1972; Swann et al. 1972) likely form in a loose regolith where diffuse transport and deposition of material is most efficient (Anderson & Anderson 2010). The wavy to linear "stair-step" EHT (ss-eht) likely forms in the active transport layer of steep slopes ≥ 20° where regolith mobility is high (Anderson & Anderson 2010). EHT on flat surfaces (≤ 3°) occurred less than ~500 m from the landform base. All of this suggests that as material moves downslope both vertically and laterally, it forms crested segments of EHT. In Section 4**,** we discuss the factors that most likely form and "preserve" EHT over time.

3.3 Comparisons between Illuminated vs. Permanently Shadowed Terrain

Illuminated and permanently shadowed terrain within the 5 km by 5 km map cells have similar areal coverage but differ slightly in surface age (88% of non-PSRs and 73% of PSRs are pre-Nectarian) and slope distribution (Fig. 9). When comparing EHT in Pre-Nectarian terrain only, we see that the frequency of EHT occurrence in PSRs is similar to that of the illuminated surface. EHT is present across all surface ages in the map area (Pre-Nectarian to Eratosthenian). We mapped more EHT in non-PSRs (81%) than in PSRs (53%). We posit that this difference is due to a higher distribution of near-horizontal surfaces on large permanently shadowed crater floors, as surfaces devoid of EHT are most likely to occur on slopes ≤ 5° (Fig. 9).

Using the ANOVA results, we found that median slope varies significantly between PSR and non-PSR cells only for unit p-eht (p-value = 0.006), while the median slope for the remaining geomorphic units showed no significant difference (p-value = 0.2 to 0.9) between PSRs and non-PSRs. An explanation as to why we do not see prominent EHT (p-eht) at slopes ≥ 15° in PSRs than at the same slopes in non-PSRs (Fig. 9) could be because wavy stair-step textures (unit ss-eht) can resemble unit p-eht at slopes ≥ 15° (Section 3.2; Fig. 9). It is possible that we mapped stair-step textures (unit ss-eht) instead of unit p-eht at slopes ≥

15°, indicating that prominent EHT likely occurs at slopes of 15° to 20° in PSRs. Using the slope frequency results, we also found that units p-eht and m-eht occur on shallow slopes ≤ 5° and median slopes 6° to 14° in both non-PSRs and PSRs (10% frequency difference), which suggests that the regolith properties in PSRs that are relevant to EHT formation are not significantly different from those of the illuminated surface (Fig. 9(a)).

Additionally, we find that segment widths between units p-eht and m-eht did not significantly vary across PSR temperature boundaries (90° to 200° change in temperature) or from PSR to PSR (Fig. 9(b)), which we would expect if temperature was correlated with EHT morphology. We also did not observe a relationship between EHT occurrence and temperature gradients due to local shadowing, as EHT did not display a pole-facing or equator-facing distribution pattern. All this suggests that illuminated and permanently shadowed terrains have similar surface morphologies, consistent with the results of Bernhardt et al. (2022) and Basilevsky et al. (2024).

3.4 Morphometric Analysis

The EHT segments that we digitized ranged from 40 to 300 m in length (long axis) and 18 to 150 m in width (short axis) at our two areas of interest (Section 2.2). EHT at the unnamed illuminated area near –88.047°S, 327.892°E (Fig. 1) displayed larger lobate segments compared to EHT on Sverdrup mound (Fig. 7) with median L/W of 120/62 vs. 81/34 m. The mound on the floor of Sverdrup crater shows varying EHT morphologies as a function of slope position. For example, a subdued EHT occurs on convex surfaces of the mound (summit to shoulder; 3° to 5° slopes), and transitions into a higher intensity EHT on the slope pediment to near flat surfaces on the foot of the slope (Fig. 7). At the unnamed illuminated site, both linear and lobate prominent EHT segments occur on a degraded crater's shoulder to inner wall (median slopes 8° to 9°). We posit that hillslope position and curvature affect the segment sizes of EHT at the two sites, given that we observed subdued EHT commonly on convex slopes (Fig. 10) and prominent EHT at the foot of slope pediments in and out of PSRs (Fig. 11(a)–11(c) and Fig. 12). As described earlier, diffuse lighting did not affect our ability to identify the textures (Fig. 11(c) and 11(d)).

The high-intensity EHT segments on Sverdrup mound are unique in our grid-map area (the most similar EHT morphology in a non-PSR is shown in Fig. 11(c) and 11(d)). To find a non-PSR texture analog, we searched ShadowCam images of equatorial craters partially in shadow to simulate indirect lighting conditions. We selected the ShadowCam image of Weber crater (50.163°N, 236.017°E) that most closely matched the PSR lighting geometry based on Weber crater's comparable geology with Sverdrup. When we compared the EHT in the ShadowCam image to co-located LROC NAC large-incidence angle images, we found no significant differences in morphology (Fig. 12). This suggests that EHT morphologies (L/W and slope) are similar across PSR to non-PSR terrain and across different latitudes.

3.4.1 Characteristic Scale of EHT-associated Topography

To derive a lower-limit height of surficial EHT using the ShadowCam DEM (with 1 to 2 m of uncertainty), we assume a uniform bedding surface and a lobate profile to create a triangle in which to measure segment length and height (Fig. 13). To do this, we collected x, y, and z data points at three positions on each segment (the base and summit), given sharp EHT segments in the DEM orthophoto (M016822289S). Note that the EHT segment base measurements may not represent the whole extent of a deformable EHT-layer thickness. Next, we used the x, y, and z distances between the points to obtain the length of each segment side using the Euclidean distance formula. Then, we derived the height of the triangle for each surficial segment:

$$height = h = \frac{2\sqrt{s(s-A)(s-B)(s-C)}}{c}$$

where s is:

$$s = \frac{(A+B+C)}{2}$$

The EHT segments that we derived to be roughly 2 to 5 m tall correspond with a lobate elevation profile in the ShadowCam 6-meter/pixel DEM (Figs. 7 and 13). Some EHT segments estimated to be < 2 m tall were resolvable in profile; however, we did not interpret them in cross section because these features are at the limit of the DEM uncertainty and were not identifiable in one of our ShadowCam images (Fig. 5(b)). To interpret the resolvable EHT segments in cross section, we assume a uniform bedding surface on a linear, diffusive hillslope, where the contact between two EHT segments represents the surface (Fig. 13). When we fit this shape in cross section to the resolvable EHT on Sverdrup mound, we find the lower limit of surficial EHT height to be 0.5 m (Fig. 7). Thus, we roughly estimate that the regolith

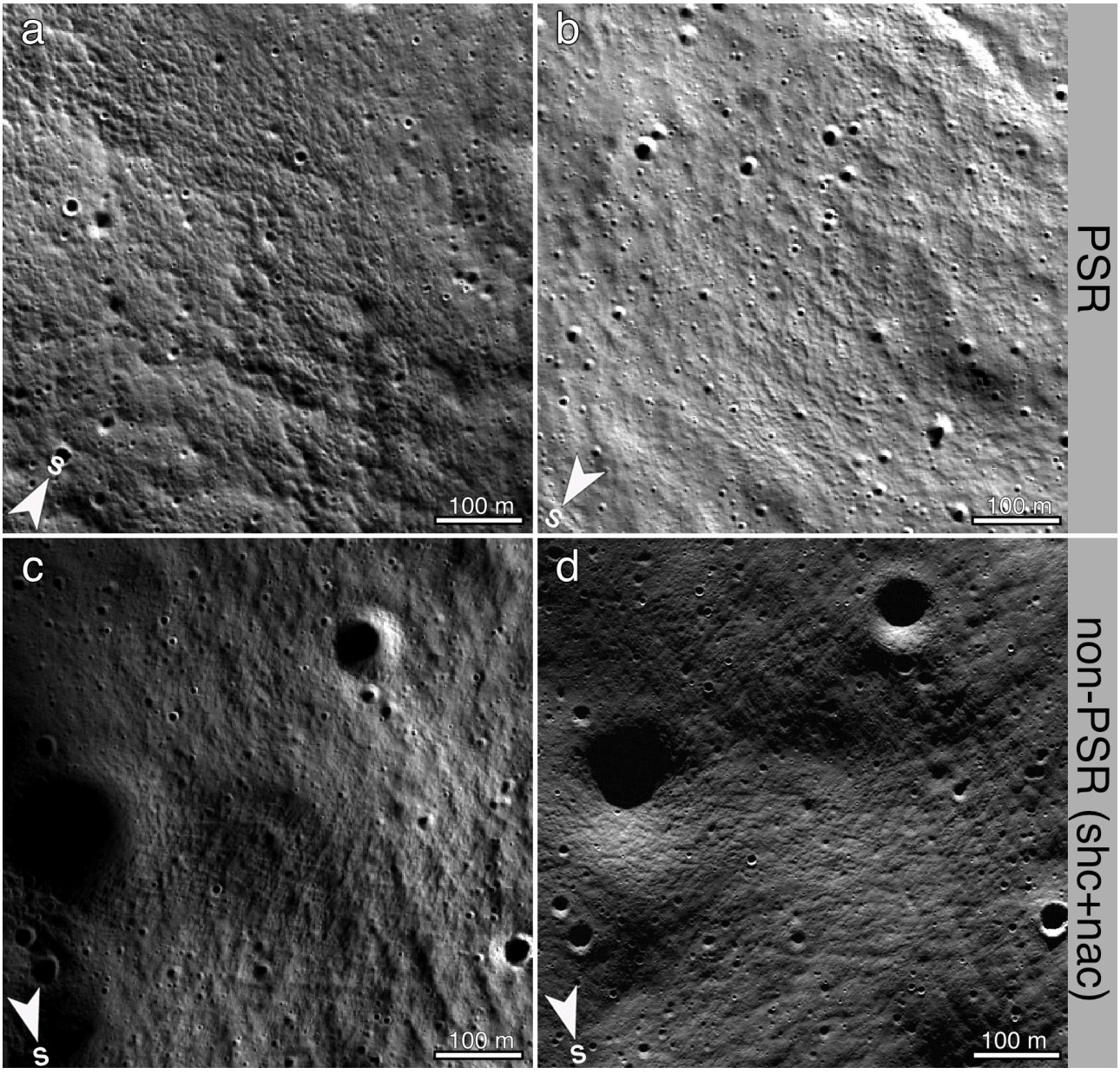

Fig. 11. High-intensity "elephant hide" texture (EHT) at the foot of slope pediments in the grid-map area. Lobate segments range from ~20 to 50 meters-wide. Median slopes are 2° to 3° for the permanently shadowed regions (PSRs) and 6° for the non-PSR. (a) Mound on the floor of Sverdrup crater (–88.332°S, 211.907°E) as shown in Fig. 7; M017013206S). (b) Shoemaker crater floor on the pediment of crater Tooley (–88.196°S, 47.241°E; M013142827S). (c) Temporarily shadowed terrain (–89.556°S, 346.891°E) observed by ShadowCam (M015613050S). (d) Same area as panel (c) but under primary illumination (LROC NAC) 1-meter/pixel mosaic (subsolar azimuth 5°). ShadowCam images are 2- meter/pixel.

layer deformed by EHT is at least 0.5 to 5 m thick (with 1 to 2 m of uncertainty on the upper limit). It is possible that the deformable EHT layer may extend below the mapped surface expression of the EHT segment base (Fig. 13 and Supplementary Fig. S1), potentially reaching depths of ~10 m, or up to the depth of the highland regolith column (Heiken et al. 1991). We did not derive EHT height estimates elsewhere in the map area due to the lack of meter-scale DEMs needed to resolve EHT topography.

4. DISCUSSION

4.1 Classic Topographic Diffusion Models do not Explain the Persistence of EHT

Classic models of landscape evolution on airless bodies predict that small-scale topographic features like EHT are short-lived (10 to 100 Ma) due to small primary impacts that smooth surface topography over time (Culling 1960; Ross

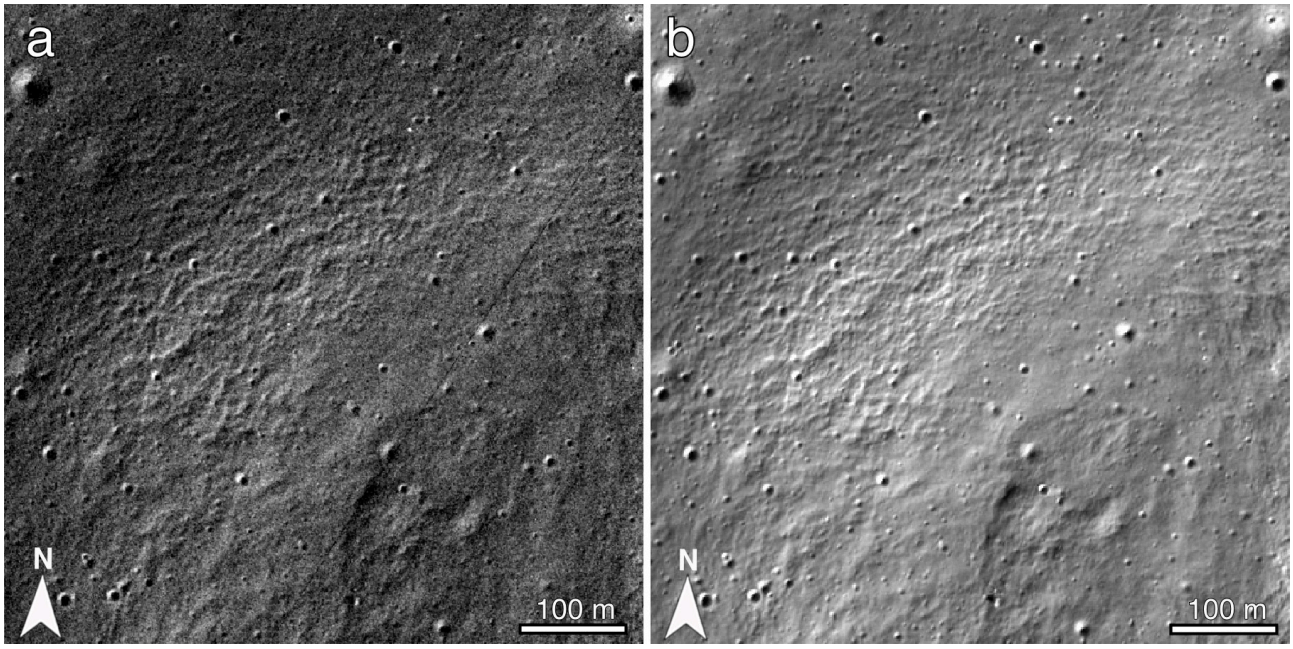

Fig. 12. Mound on the floor of Weber crater (50.163°N, 236.017°E) showing "elephant hide" texture (EHT) morphology. (a) ShadowCam image (M086369576S) taken when the equatorial crater was in temporary shadow. (b) Lunar Reconnaissance Orbiter Camera Narrow Angle Camera (LROC NAC) images M1109074783LR with incidence angle 83°.

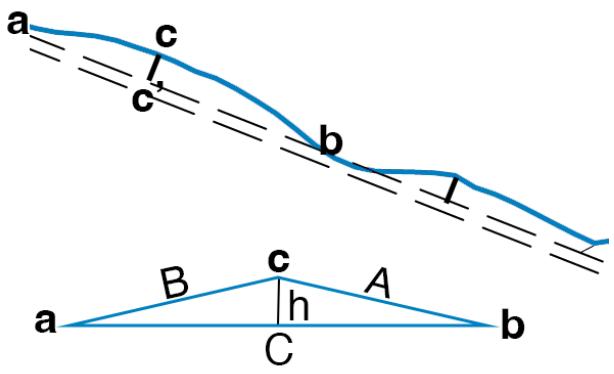

Fig. 13. Cross-section (from Fig. 7, B to B') showing where we collected location (x, y) and elevation (z) values at three positions (a, b, and c) along an "elephant hide" texture (EHT) segment. The distances between points (A, B, and C) are used to estimate the lower-limit height (h) of a surficial EHT segment at its highest elevation point (c). We assume a uniform bedding surface and a surficial lobate profile to derive the characteristic scale of EHT-associated topography.

1968; Soderblom 1970; Pelletier 2008; Fassett & Thomson 2014). Recent workers have shown that nonlinear diffusion (scale- and slope-dependent erosion and transport) more accurately models the observed equilibrium populations of lunar craters (Speyerer et al. 2016; Minton et al. 2019; Fassett et al. 2022; O'Brien & Byrne 2022). However, modern topographic diffusion models still do not explain the persistence of EHT (Gold & Williams 1973; Houston et al. 1973; Kreslavsky et al. 2021, 2023). It is possible that the diffusion parameter in these models (Minton et al. 2019; Fassett et al. 2022; O'Brien & Byrne 2022) may not adequately capture EHT-scale features or may misrepresent the dominant processes that form them (Houston et al. 1973; Kreslavsky et al. 2023).

The presence of both subdued and prominent EHT across similar slopes indicates that diffusion of material must vary nonlinearly, consistent with findings from Kreslavsky et al. (2023) and O'Brien & Byrne (2022). Modern diffusion models are limited to predictions of how material moves at the surface (Li & Mustard 2000). Multiple factors that could constrain the survivability of EHT on the surface remain unaccounted for, including movement of particles at depth, degree of compaction, cohesion, and particle sorting (O'Brien & Byrne 2022). As such, an explanation for the variation of EHT across slopes is that heterogeneous subsurface regolith properties influence transport and affect how the mobile segments of EHT form at the surface. It is also likely that regolith creep driven by periodic seismic shaking contribute to variations of EHT across the surface.

4.2 Alternatives to Micrometeoroid Diffusion

4.2.1 Thermal Erosion

Thermal cycling contributes to regolith formation on

airless bodies (Ross 1968; Delbo et al. 2014; Molaro et al. 2015, 2017) and drives subsequent creep (Duennebier 1976; Melosh 2011; Bovie et al. 2023). However, it is still unclear how long-term thermal cycling drives creep on the Moon. Thermal cycling at the diurnal timescale is strongest in the top few centimeters of regolith (Hayne et al. 2017; Bovie et al. 2023), and temperature variations over millions of years may penetrate to a depth of ~1.5 to 2 m (Langseth et al. 1972; Anderson & Anderson 2010). Across the lunar surface, diurnal temperature amplitude varies significantly with latitude, slope orientation, and topographic shadowing (Bandfield et al. 2011, 2015; Gläser et al. 2021). If thermal cycling drives EHT-related movement, we would expect to see differences in EHT near the equator relative to polar regions, in local equatorial slopes (with the highest temperature amplitude), and within seasonally shadowed regions near the poles. However, previous work has shown no significant difference in the global distribution of EHT (Xiao et al. 2013; Kreslavsky et al. 2021; Bondarenko et al. 2022).

Multiple studies postulate that PSRs have less compacted regolith (high porosity and/or reduced cohesion) (Hayne et al. 2017; Metzger et al. 2018; Bürger et al. 2024) in the upper few centimeters when compared to non-PSR terrain due to smaller thermal amplitudes (Williams et al. 2019). Given this, one would expect that loose regolith on shallow slopes in PSRs would be more easily mobilized. We did not observe evidence of this, however. Currently, thermal cycling experiments have only shown how terrestrial granular materials (Divoux 2010) and lunar regolith (Metzger et al. 2018) behave under a short-term laboratory environment. The delta temperature threshold required for long-term thermal erosion and deposition of ancient lunar soils is unknown. Since PSRs are thought to have lower regolith thermal expansion (due to minimal temperature variations) in comparison to non-PSRs, we mapped the frequency of occurrence of EHT across PSR to non-PSR temperature boundaries (90° to 200° change in temperature; Fig. 9) to search for a change in EHT. We found that geomorphic units occur at all temperatures across these boundaries (Supplementary Fig. S2), indicating that thermal cycling does not play a key role in EHT formation.

4.2.2 Moonquakes

Periodic seismic shaking induced by secondary impacts, tidal stresses, and global contraction due to interior cooling likely contribute to variations of EHT across the surface. Experiments show that vibrations both compact and re-loosen regolith depending on vibration amplitude (amplitudes as low as ~0.02° g could cause regolith disturbance) (Divoux 2010; Gamsky & Metzger 2010; Metzger et al. 2018; Watters et al. 2024, Schmerr et al. 2025). We can infer that seismic shaking could both form and degrade EHT, especially on steep slopes and areas with low cohesion (Antonenko 2012; Watters & Schmerr 2025). Heterogeneity in the subsurface geology could also influence seismic wave propagation (Schmerr et al. 2025). This may be another explanation for the variation of EHT across slopes. If seismic shaking due to tectonic stresses periodically drives EHT formation, we might expect to see morphologic evidence of disturbed regolith near the thousands of globally distributed fault scarps (Watters et al. 2015; Watters et al. 2024), perhaps even up to 30 km from a young surface quake epicenter (Kumar et al. 2019; Watters et al. 2019). We did not observe evidence of this in our map area, however. More research is needed to understand how lunar seismic shaking disturbs regolith on flat surfaces to create EHT.

4.3 What do other Airless Bodies Tell us about EHT on the Moon?

EHT has been observed on one other airless body, Mercury. Using Mercury Dual Imaging System (MDIS) (Hawkins et al. 2007) images at < 2.5 m/pixel, Zharkova et al. (2020) found that EHT segments on Mercury are less abundant and up to ~8 times shorter than on the Moon. The authors posit that this may be due to increased rates of topographic diffusion in comparison to the Moon (Cintala 1992; Braden & Robinson 2013; Fassett et al. 2017) and, therefore, small-scale features degrade faster than they are produced or are in equilibrium (Zharkova et al. 2020). Mercury has a higher daytime temperature and thermal amplitude than the Moon (Morrison 1970), which could potentially affect the development of EHT (Zharkova et al. 2020). Also, differences in mineral composition and physical particle properties between the regolith of the Moon and Mercury are unknown and might cause significant variations. A global Mercury dataset of images with sufficient resolution to reveal EHT is needed to test these hypotheses (Zharkova et al. 2020).

The potential occurrence of EHT on the dwarf planet Ceres and on numerous asteroids has yet to be thoroughly investigated. Images taken by the Dawn spacecraft during low altitude orbit (35-meter/pixel scale) reveal landscapes likely shaped by impact, tectonic, and cryogenic processes (Buczkowski et al. 2016; Roatsch et al. 2016). Several studies show evidence for loose regolith on Ceres (Schmidt et al. 2017; Palmer et al. 2021), perhaps even 15% more porous

than regolith on the Moon (Palmer et al. 2021). Similarly, centimeters-to-meters-scale images of asteroids Bennu, Ryugu, Eros, and Vesta reveal evidence of mass wasting of loose material likely driven by similar (anhydrous) processes to the Moon (Heiken et al. 1991; Robinson et al. 2002; Buczkowski et al. 2014; Lauretta et al. 2019; Sugita et al. 2019; Walsh et al. 2022). A loosely packed and less cohesive regolith likely plays a role in EHT formation, so observations of textures analogous to EHT on these bodies would be fruitful to understanding its formation. Another reason why EHT has not been documented on asteroids and comets could be because of the young surface age (~100 to ~200 million years). However, more work is needed to understand how EHT varies with surface age on the Moon.

5. CONCLUSIONS

Our grid-mapping near the lunar south pole (90°S to 88°S) constrain where patterned regolith textures are most likely to form. Mapping and spatial analysis presented here show that:

1. Diffuse lighting does not interfere with our ability to identify EHT. This finding helps guide the interpretation of PSR landforms in terms of regolith strength properties, which could be affected by the presence of water ice.
2. Regolith properties in PSRs that are relevant to EHT formation are not significantly different from those of the illuminated surface. We mapped EHT morphology across PSR to non-PSR temperature boundaries (90° to 200° change in temperature) and found that EHT units have a similar likelihood to occur across polar terrains (up to 10% frequency difference) regardless of median slope and temperature. Thermal amplitudes as low as 1° to ~20° can induce regolith creep through short-term thermal cycling (Divoux 2010; Metzger et al. 2018), however, our results suggest that thermal cycling is not a key driver of EHT movement.
3. Distance from a hillcrest and landscape curvature affect EHT morphology. For example, EHT is most pronounced on the talus and toe of slopes, and subdued EHT typically form on convex surfaces. We found EHT on nearly-horizontal surfaces (slopes ≤ 3°) only less than ~500 m from the landform base. These observations show that EHT formation is in part controlled by slope, consistent with previous work (Swann et al. 1972; Plescia & Robinson 2010; Xiao et al. 2013; Kreslavsky et al. 2021; Bernhardt et al. 2022; Bondarenko et al. 2022; Brown et al. 2025).
4. The upper 0.5 to 1 m of regolith may act like a blanket that creeps downhill continuing onto horizontal surfaces to form crested and cohesive segments. We observed variation of EHT morphology across the same slopes; this suggests that EHT is both formed and degraded by periodic, vibration- amplitude-dependent disturbances such as tidal stresses and global contraction due to interior cooling.

A global map of EHT would help to further constrain locations of EHT occurrences and understand how it varies with surface age, geologic terrain, and proximity to young tectonic features and impacts. The geomorphic units we mapped (within cells 1 km by 1 km; 5 km by 5 km) could serve as a test dataset to train a feature classification machine learning model. This future work will add to our current understanding of EHT, but the mapping presented here offers valuable parameters to improve EHT formation models, which in turn inform aspects of future landed exploration, like hazard avoidance and regolith stability.

ACKNOWLEDGMENTS

We would like to thank Robert Wagner, Madeleine Manheim, Torie Roseborough, Prasun Mahanti, and Patrick O'Brien for their valuable feedback and fruitful discussions about elephant hide texture. We also thank Mikhail Kreslavsky for a thoughtful review which improved the clarity of this work. This work was supported by the National Aeronautics and Space Administration Lunar Reconnaissance Orbiter and ShadowCam projects.

ORCIDs

Holly M. Brown https://orcid.org/0000-0001-9329-8464
Aaron K. Boyd https://orcid.org/0000-0002-5974-9919
Mark S. Robinson https://orcid.org/0000-0001-9964-2932
Megan R. Henriksen https://orcid.org/0000-0001-6993-4774
Hannes Bernhardt https://orcid.org/0000-0002-6461-033X

SUPPLEMENTARY MATERIALS

Supplementary materials are only available online from: https://doi.org/10.5140/JASS.2026.43.1.1

REFERENCES

Anderson RS, Anderson SP, Geomorphology: The Mechanics and Chemistry of Landscapes (Cambridge University Press, Cambridge, UK, 2010).

Antonenko I, Leathery texture in the Bose, Bhabha, and Stoney crater region of South Pole-Aitken basin on the Moon, in 43rd Annual Lunar and Planetary Science Conference, The Woodlands, TX, 19-23 Mar 2012.

Archinal BA, Weller LA, Richie JO, Lee EM, Bennett KA, et al., Controlled high-resolution LROC NAC polar mosaics, in 54th Lunar and Planetary Science Conference, The Woodlands, TX, 13-17 Mar 2023.

Bandfield JL, Ghent RR, Vasavada AR, Paige DA, Lawrence SJ, et al., Lunar surface rock abundance and regolith fines temperatures derived from LRO Diviner Radiometer data, J. Geophys. Res. Planets. 116, E00H02 (2011). https://doi.org/10.1029/2011JE003866

Bandfield JL, Hayne PO, Williams JP, Greenhagen BT, Paige DA, Lunar surface roughness derived from LRO Diviner Radiometer observations, Icarus. 248, 357-372 (2015). https://doi.org/10.1016/j.icarus.2014.11.009

Barker MK, Mazarico E, Neumann GA, Smith DE, Zuber MT, et al., Improved LOLA elevation maps for South pole landing sites: error estimates and their impact on illumination conditions, Planet. Space Sci. 203, 105119 (2021). https://doi.org/10.1016/j.pss.2020.105119

Basilevsky AT, Krasilnikov SS, Li Y, Photogeological analysis of ShadowCam images of the permanently shadowed floor of lunar crater Shoemaker, Planet. Space Sci. 254, 105998 (2024). https://doi.org/10.1016/j.pss.2024.105998

Bernhardt H, Robinson MS, Boyd AK, Geomorphic map and science target identification on the Shackleton-de Gerlache ridge, Icarus 379, 114963 (2022). https://doi.org/10.1016/j.icarus.2022.114963

Bondarenko NV, Dulova IA, Kornienko YV, High-resolution albedo and relief of the lunar surface with the improved photoclinometry method for the topography reconstruction from a set of images, in 49th Annual Lunar and Planetary Science Conference, The Woodlands, TX, 19-23 Mar 2018.

Bondarenko NV, Kreslavsky MA, Zubarev A, Nadezhdina I, "Elephant hide" texture on the Moon: preliminary results on topographic properties, in 53rd Lunar and Planetary Science Conference, The Woodlands, TX, 7-11 Mar 2022.

Bondarenko NV, Possible lack of small craters in "elephant hide" areas on the Moon: a case study, in 54th Lunar and Planetary Science Conference, The Woodlands, TX, 13-17 Mar 2023.

Bovie D, Quillen AC, Glade R, Rearrangement of granular surfaces on asteroids due to thermal cycling (2023) [Internet], viewed 2025 Oct 20, available from: https://doi.org/10.48550/arXiv.2308.03749

Braden SE, Robinson MS, Relative rates of optical maturation of regolith on Mercury and the Moon, J. Geophys. Res. Planets. 118, 1903-1914 (2013). https://doi.org/10.1002/jgre.20143

Brown HM, Boyd AK, Denevi BW, Henriksen MR, Manheim MR, et al., Resource potential of lunar permanently shadowed regions, Icarus. 377, 114874 (2022). https://doi.org/10.1016/j.icarus.2021.114874

Brown HM, Boyd AK, Henriksen MR, Bernhardt H, Grid-mapping of elephant hide textures near the lunar south pole, in 56th Lunar and Planetary Science Conference, The Woodlands, TX, 10-14 Mar 2025.

Brown HM, Wagner RV, Robinson MS, Viewing geometry and slope effects on the identification of lunar elephant hide texture, in 55th Lunar and Planetary Science Conference, The Woodlands, TX, 11-15 Mar 2024.

Buczkowski DL, Schmidt BE, Williams DA, Mest SC, Scully JEC, et al., The geomorphology of Ceres, Science. 353, aaf4332 (2016). https://doi.org/10.1126/science.aaf4332

Buczkowski DL, Wyrick DY, Toplis M, Yingst RA, Williams DA, et al., The unique geomorphology and physical properties of the Vestalia Terra plateau, Icarus. 244, 8-03 (2014). https://doi.org/10.1016/j.icarus.2014.03.035

Bürger J, Hayne PO, Gundlach B, Läuter M, Kramer T, et al., A microphysical thermal model for the lunar regolith: investigating the latitudinal dependence of regolith properties, J. Geophys. Res. Planets. 129, e2023JE008152 (2024). https://doi.org/10.1029/2023JE008152

Cintala MJ, Impact-induced thermal effects in the lunar and Mercurian regoliths, J. Geophys. Res. Planets. 97, 947-973 (1992). https://doi.org/10.1029/91JE02207

Conrad O, Bechtel B, Bock M, Dietrich H, Fischer E, et al., System for automated geoscientific analyses (SAGA) v. 2.1.4, Geosci. Model Dev. 8, 1991-2007 (2015). https://doi.org/10.5194/gmd-8-1991-2015

Crittenden MD, Terrestrial analogues of lunar mass wasting, Preliminary geologic evaluation and Apollo landing analysis of areas photographed by Lunar Orbiter III, NASA Langley Research Center Working Paper 407, 125-127 (1967).

Culling WEH, Analytical theory of erosion, J. Geol. 68, 336-344 (1960). https://doi.org/10.1086/626663

Delbo M, Libourel G, Wilkerson J, Murdoch N, Michel P, et al., Thermal fatigue as the origin of regolith on small asteroids, Nature. 508, 233-236 (2014). https://doi.org/10.1038/nature13153

Divoux T, Invited review: effect of temperature on a granular pile, Pap. Phys. 2, 020006 (2010). https://doi.org/10.4279/pip.020006

Duennebier FR, Thermal movement of the regolith, vol. 1, 7th Lunar Science Conference (Pergamon Press, New York, UK,

1976), 1073-1086.

Edmundson KL, Cook DA, Thomas OH, Archinal BA, Kirk RL, Jigsaw: the ISIS3 bundle adjustment for extraterrestrial photogrammetry, ISPRS Ann. Photogramm. Remote Sens. Spatial Inf. Sci. I-4, 203-208 (2012). https://doi.org/10.5194/isprsannals-I-4-203-2012

Fassett CI, Beyer RA, Deutsch AN, Hirabayashi M, Leight CJ, et al., Topographic diffusion revisited: small crater lifetime on the Moon and implications for volatile exploration, J. Geophys. Res. Planets. 127, e2022JE007510 (2022). https://doi.org/10.1029/2022JE007510

Fassett CI, Crowley MC, Leight C, Dyar MD, Minton DA, et al., Evidence for rapid topographic evolution and crater degradation on Mercury from simple crater morphometry, Geophys. Res. Lett. 44, 5326-5335 (2017). https://doi.org/10.1002/2017GL073769

Fassett CI, Thomson BJ, Crater degradation on the lunar maria: topographic diffusion and the rate of erosion on the Moon, J. Geophys. Res. Planets. 119, 2255-2271 (2014). https://doi.org/10.1002/2014JE004698

Fortezzo CM, Spudis PD, Harrel SL, Release of the digital unified global geologic map of the Moon at 1: 5,000,000-scale, in 51st Annual Lunar and Planetary Science Conference, The Woodlands, TX, 16-20 Mar 2020.

Gamsky JN, Metzger PT, The physical state of lunar soil in the permanently shadowed craters of the Moon, Earth and Space 2010: Engineering, Science, Construction, and Operations in Challenging Environments, eds. Song G, Malla RB (ASCE Library, Reston, VA, 2010), 260-265.

GDAL/OGR contributors, GDAL/OGR Geospatial data abstraction software library (2025) [Internet], available from: https://doi.org/10.5281/zenodo.5884351

Gläser P, Sanin A, Williams JP, Mitrofanov I, Oberst J, Temperatures near the lunar poles and their correlation with hydrogen predicted by LEND, J. Geophys. Res. Planets. 126, e2020JE006598 (2021). https://doi.org/10.1029/2020JE006598

Gold T, Williams GJ, Electrostatic transportation of dust on the Moon, in Photon and Particle Interactions with Surfaces in Space, eds. Grard RJL (Springer, Dordrecht, Nederlands, 1973).

Greeley R, Lava tubes and channels in the lunar Marius Hills, The Moon. 3, 289-314 (1971). https://doi.org/10.1007/BF00561842

Haruyama J, Ohtake M, Matsunaga T, Morota T, Honda C, et al., Lack of exposed ice inside lunar south pole Shackleton crater, Science. 322, 938-939 (2008). https://doi.org/10.1126/science.1164020

Hawkins SE III, Boldt JD, Darlington EH, Espiritu R, Gold RE, et al., The Mercury dual imaging system on the MESSENGER spacecraft, Space Sci. Rev. 131, 247-338 (2007). https://doi.org/10.1007/s11214-007-9266-3

Hayne PO, Bandfield JL, Siegler MA, Vasavada AR, Ghent RR, et al., Global regolith thermophysical properties of the Moon from the Diviner Lunar Radiometer Experiment, J. Geophys. Res. Planets. 122, 2371-2400 (2017). https://doi.org/10.1002/2017JE005387

Heiken G, Vaniman D, French BM, Lunar Sourcebook: A User's Guide to the Moon (Cambridge University Press, Cambridge, UK, 1991).

Horn BKP, Hill shading and the reflectance map, Proc. IEEE 69, 14-47 (1981). https://doi.org/10.1109/PROC.1981.11918

Houston WN, Moriwaki Y, Chang CS, Downslope movement of lunar soil and rock caused by meteoroid impact, in Fourth Lunar Science Conference, Houston, TX, 5-8 Mar 1973.

Howard KA, Larsen BR, Lineaments that are artifacts of lighting, Part G, Manned Spacecraft Center Apollo 15 Preliminary Science Report, NASA/19720015195 (1972).

Kienzle S, The effect of DEM raster resolution on first order, second order and compound terrain derivatives, Trans. GIS. 8, 83-111 (2004). https://doi.org/10.1111/j.1467-9671.2004.00169.X

Kreslavsky MA, Bondarenko NV, Head JW, Ubiquity of "Elephant hide" texture on the Moon, in 52nd Lunar and Planetary Science Conference, The Woodlands, TX, 15-19 Mar 2021.

Kreslavsky MA, Zubarev A, Nadezhdina I, Bondarenko N, Non-diffusive regolith transport on the Moon, in 54th Lunar and Planetary Science Conference, The Woodlands, TX, 13-17 Mar 2023.

Kuiper GP, Interpretation of Ranger VII records, in Ranger VII Part II: Experimenters' Analyses and Interpretations, NASA Jet Propulsion Laboratory Technical Report 32-700, 9-73 (1965).

Kumar PS, Mohanty R, Lakshmi KJP, Raghukanth STG, Dabhu AC, et al., The seismically active lobate scarps and coseismic lunar boulder avalanches triggered by 3 January 1975 (MW 4.1) shallow moonquake, Geophys. Res. Lett. 46, 7972-7981 (2019). https://doi.org/10.1029/2019GL083580

Langseth MG Jr, Clark SP Jr, Chute JL Jr, Keihm SJ, Wechsler AE, The Apollo 15 lunar heat-flow measurement, The Moon. 4, 390-410 (1972). https://doi.org/10.1007/BF00562006

Lauretta DS, DellaGiustina DN, Bennett CA, Golish DR, Becker KJ, et al., The unexpected surface of asteroid (101955) Bennu, Nature. 568, 55-60 (2019). https://doi.org/10.1038/s41586-019-1033-6

Lena R, Fitzgerald B, On a volcanic construct and a lunar pyroclastic deposit (LPD) in northern Mare Vaporum, Planet. Space Sci. 92, 1-15 (2014). https://doi.org/10.1016/j.pss.2014.01.012

Li L, Mustard JF, Compositional gradients across mare-highland contacts: importance and geological implication of lateral transport, J. Geophys. Res. Planets. 105, 20431-20450 (2000). https://doi.org/10.1029/1999JE001168

Mahanti P, Robinson MS, Humm DC, Wagner RV, Estes NM, et al., Preliminary characterization of secondary illumination at Shackleton crater permanently shadowed region from ShadowCam observations and modeling, J. Astron. Space Sci. 40, 131-148 (2023). https://doi.org/10.5140/JASS.2023.40.4.131

Mahanti P, Thompson TJ, Robinson MS, Humm DC, View factor-based computation of secondary illumination within lunar permanently shadowed regions, IEEE Geosci. Remote Sens. Lett. 19, 1-4 (2022). https://doi.org/10.1109/LGRS.2022.3166809

Mahanti P, Williams JP, Robinson MS, Wagner R, Mazarico E, et al., Dynamic secondary illumination in permanent shadows within Artemis III candidate landing regions, Planet. Sci. J. 5, 62 (2024). https://doi.org/10.3847/PSJ/ad1b50

Manheim MR, Henriksen MR, Wagner RV, Michaud CH, ShadowCam Team, ShadowCam digital terrain models of permanently shadowed regions, in 55th Lunar and Planetary Science Conference, The Woodlands, TX, 11-15 Mar 2024.

Martin AC, Denevi BW, Speyerer EJ, Boyd AK, Brown HM, Imaging in shadows: a comparison of craters observed in primary and secondary illumination with the Lunar Reconnaissance Orbiter Camera, Planet. Sci. J. 5, 207 (2024). https://doi.org/10.3847/PSJ/ad6005

Mattingly TK, El-Baz F, Laidley RA, Observations and impressions from lunar orbit, Apollo 16 Preliminary Science Report, NASA/19730013037 (1972).

Mazarico E, Neumann GA, Smith DE, Zuber MT, Torrence MH, Illumination conditions of the lunar polar regions using LOLA topography, Icarus. 211, 1066-1081 (2011). https://doi.org/10.1016/j.icarus.2010.10.030

Melosh HJ, Planetary Surface Processes (Cambridge University Press, Cambridge, UK, 2011).

Metzger PT, Anderson S, Colaprete A, Experiments indicate regolith is looser in the lunar polar regions than at the lunar landing sites, in Earth and Space 2018: Engineering for Extreme Environments, eds. Malla RB, Goldberg RK, Roberts AD (ASCE Library, Reston, VA, 2018).

Minton DA, Fassett CI, Hirabayashi M, Howl BA, Richardson JE, The equilibrium size-frequency distribution of small craters reveals the effects of distal ejecta on lunar landscape morphology, Icarus. 326, 63-87 (2019). https://doi.org/10.1016/j.icarus.2019.02.021

Mitusov AV, Stark A, Khrisanov VR, Oberst J, Hidden morphology of Shackleton Crater, lunar south pole, Planet. Space Sci. 238, 105795 (2023). https://doi.org/10.1016/j.pss.2023.105795

Molaro JL, Byrne S, Langer SA, Grain-scale thermoelastic stresses and spatiotemporal temperature gradients on airless bodies, implications for rock breakdown, J. Geophys. Res. Planets. 120, 255-277 (2015). https://doi.org/10.1002/2014JE004729

Molaro JL, Byrne S, Le JL, Thermally induced stresses in boulders on airless body surfaces, and implications for rock breakdown, Icarus. 294, 247-261 (2017). https://doi.org/10.1016/j.icarus.2017.03.008

Morrison D, Thermophysics of the planet Mercury, Space Sci. Rev. 11, 271-307 (1970). https://doi.org/10.1007/BF00241524

O'Brien P, Byrne S, Degradation of the lunar surface by small impacts, Planet. Sci. J. 3, 235 (2022). https://doi.org/10.3847/PSJ/ac9130

Palmer EM, Heggy E, Letertre T, Sabouroux P, Exploring Ceres's unusual regolith porosity and its implications for volatile retention, Planet. Sci. J. 2, 182 (2021). https://doi.org/10.3847/PSJ/ac0b3e

Parker RA, Baldwin RR, Brett R, Fuller JD, Giesecke RL, et al., Apollo 17 Preliminary Science Report, NASA/SP-330-19740010319 (1973).

Pelletier JD, Quantitative Modeling of Earth Surface Processes (Cambridge University Press, Cambridge, UK, 2008).

Plescia J, Robinson MS, Character of the lunar regolith: the view from LROC, in European Planetary Science Congress, Rome, Italy, 19-24 Sep 2010.

QGIS Development Team, QGIS (2025) [Internet], available from: https://qgis.org/download/

Roatsch T, Kersten E, Matz KD, Preusker F, Scholten F, et al., High-resolution Ceres high altitude mapping orbit atlas derived from Dawn framing camera images, Planet. Space Sci. 129, 103-107 (2016). https://doi.org/10.1016/j.pss.2016.05.011

Robinson MS, Brylow SM, Caplinger MA, Carter LM, Clark MJ, et al., ShadowCam instrument and investigation overview, J. Astron. Space Sci. 40, 149-171 (2023). https://doi.org/10.5140/JASS.2023.40.4.149

Robinson MS, Brylow SM, Tschimmel M, Humm D, Lawrence SJ, et al., Lunar Reconnaissance Orbiter Camera (LROC) instrument overview, Space Sci. Rev. 150, 81-124 (2010). https://doi.org/10.1007/s11214-010-9634-2

Robinson MS, Thomas PC, Plescia JB, Denevi BW, Burns KN, et al., An exceptional grouping of lunar highland smooth plains: geography, morphology, and possible origins, Icarus. 273, 121-134 (2016). https://doi.org/10.1016/j.icarus.2015.06.028

Robinson MS, Thomas PC, Veverka J, Murchie SL, Wilcox BB, The geology of 433 Eros, Meteorit. Planet. Sci. 37, 1651-1684 (2002). https://doi.org/10.1111/j.1945-5100.2002.tb01157.x

Ross HP, A simplified mathematical model for lunar crater erosion, J. Geophys. Res. 73, 1343-1354 (1968). https://doi.org/10.1029/JB073i004p01343

Schaber GG, Swann GA, Surface lineaments at the Apollo 11 and Apollo 12 landing sites, Proceedings of the Lunar Science Conference, ed. Levinson AA (MIT press, Cambridge, MA, 1971), 27-38.

Schmerr NC, Frizzell E, Hartzell C, Bernhardt H, Clark J, et al., A seismic origin for lunar coldspots, in 56th Lunar and Planetary Science Conference, The Woodlands, TX, 10-14 Mar. 2025.

Schmidt BE, Hughson KHG, Chilton HT, Scully JEC, Platz T, et al., Geomorphological evidence for ground ice on dwarf planet Ceres, Nat. Geosci. 10, 338-343 (2017). https://doi.org/10.1038/ngeo2936

Shoemaker EM, Progress in the analysis of the fine structure and geology of the lunar surface from the Ranger VIII and IX photographs, in Ranger VIII and IX Part II: Experimenters' Analyses and Interpretations, NASA Jet Propulsion Laboratory Technical Report 32-800, 249-337 (1966).

Scott DR, Worden AM, Irwin JB, Crew observations. Section 4 of Apollo 15 Preliminary Science Report, NASA SP-289-19720015164 (1972).

Soderblom LA, A model for small-impact erosion applied to the lunar surface, J. Geophys. Res. 75, 2655-2661 (1970). https://doi.org/10.1029/JB075i014p02655

Speyerer EJ, Povilaitis RZ, Robinson MS, Thomas PC, Wagner RV, Quantifying crater production and regolith overturn on the Moon with temporal imaging, Nature. 538, 215-218 (2016). https://doi.org/10.1038/nature19829

Sthle L, Wold S, Multivariate analysis of variance (MANOVA), Chemometr. Intell. Lab. Syst. 9, 127-141 (1990). https://doi.org/10.1016/0169-7439(90)80094-M

Sugita S, Honda R, Morota T, Kameda S, Sawada H, et al., The geomorphology, color, and thermal properties of Ryugu: implications for parent-body processes, Science. 364, eaaw0422 (2019). https://doi.org/10.1126/science.aaw0422

Swann GA, Bailey NG, Batson RM, Freeman VL, Hait MH, et al., Preliminary geologic investigation of the Apollo 15 Landing Site, Apollo 15 Preliminary Science Report, NASA/19720015169 (1972).

The MathWorks Inc., MATLAB version: 9.13.0.2105380 (R2022b) (2022) [Internet], available from: https://www.mathworks.com/products/new_products/latest_features.html?s_tid=hp_highlights_release

Voelker M, Hauber E, Schulzeck F, Jaumann R, Grid-mapping Hellas Planitia, Mars – insights into distribution, evolution and geomorphology of (Peri)-glacial, fluvial and lacustrine landforms in Mars' deepest basin, Planet. Space Sci. 145, 49-70 (2017). https://doi.org/10.1016/j.pss.2017.07.012

Wagner RV, Speyerer EJ, Robinson MS, Cartographic accuracy of ShadowCam images, in 55th Lunar and Planetary Science Conference, The Woodlands, TX, 11-15 Mar 2024.

Walsh KJ, Ballouz RL, Jawin ER, Avdellidou C, Barnouin OS, et al., Near-zero cohesion and loose packing of Bennu's near subsurface revealed by spacecraft contact, Sci. Adv. 8, eabm6229 (2022). https://doi.org/10.1126/sciadv.abm6229

Watters TR, Robinson MS, Collins GC, Banks ME, Daud K, et al., Global thrust faulting on the Moon and the influence of tidal stresses, Geology. 43, 851-854 (2015). https://doi.org/10.1130/G37120.1

Watters TR, Schmerr NC, Paleoseismic activity in the moon's Taurus-Littrow valley inferred from boulder falls and landslides, Sci. Adv. 11, eadu3201 (2025). https://doi.org/10.1126/sciadv.adu3201

Watters TR, Schmerr NC, Weber RC, Johnson CL, Speyerer EJ, et al., Tectonics and seismicity of the lunar South polar region, Planet. Sci. J. 5, 22 (2024). https://doi.org/10.3847/PSJ/ad1332

Watters TR, Weber RC, Collins GC, Howley IJ, Schmerr NC, et al., Shallow seismic activity and young thrust faults on the Moon, Nat. Geosci. 12, 411-417 (2019). https://doi.org/10.1038/s41561-019-0362-2

Williams JP, Greenhagen BT, Paige DA, Schorghofer N, Sefton-Nash E, et al., Seasonal polar temperatures on the Moon, J. Geophys. Res. Planets. 124, 2505-2521 (2019). https://doi.org/10.1029/2019JE006028

Williams JP, Mahanti P, Robinson MS, Wagner RV, Chertok M, et al., The Faustini permanently shadowed region on the Moon, Planet. Sci. J. 5, 209 (2024). https://doi.org/10.3847/PSJ/ad6f0d

Wood J, The geomorphological characterisation of digital elevation models, PhD Dissertation, University of Leicester (1996).

Wood J, Geomorphometry in LandSerf, in Developments in Soil Science, eds. Hengl T, Reuter HI (Elsevier, Amsterdam, Nederlands, 2009), 333-349.

Xiao Z, Zeng Z, Ding N, Molaro J, Mass wasting features on the Moon: how active is the lunar surface? Earth Planet. Sci. Lett. 376, 1-11 (2013). https://doi.org/10.1016/j.epsl.2013.06.015

Zevenbergen LW, Thorne CR, Quantitative analysis of land surface topography, Earth Surf. Process. Landf. 12, 47-56 (1987). https://doi.org/10.1002/esp.3290120107

Zharkova AY, Kreslavsky MA, Head JW, Kokhanov AA, Regolith textures on Mercury: comparison with the Moon, Icarus. 351, 113945 (2020). https://doi.org/10.1016/j.icarus.2020.113945

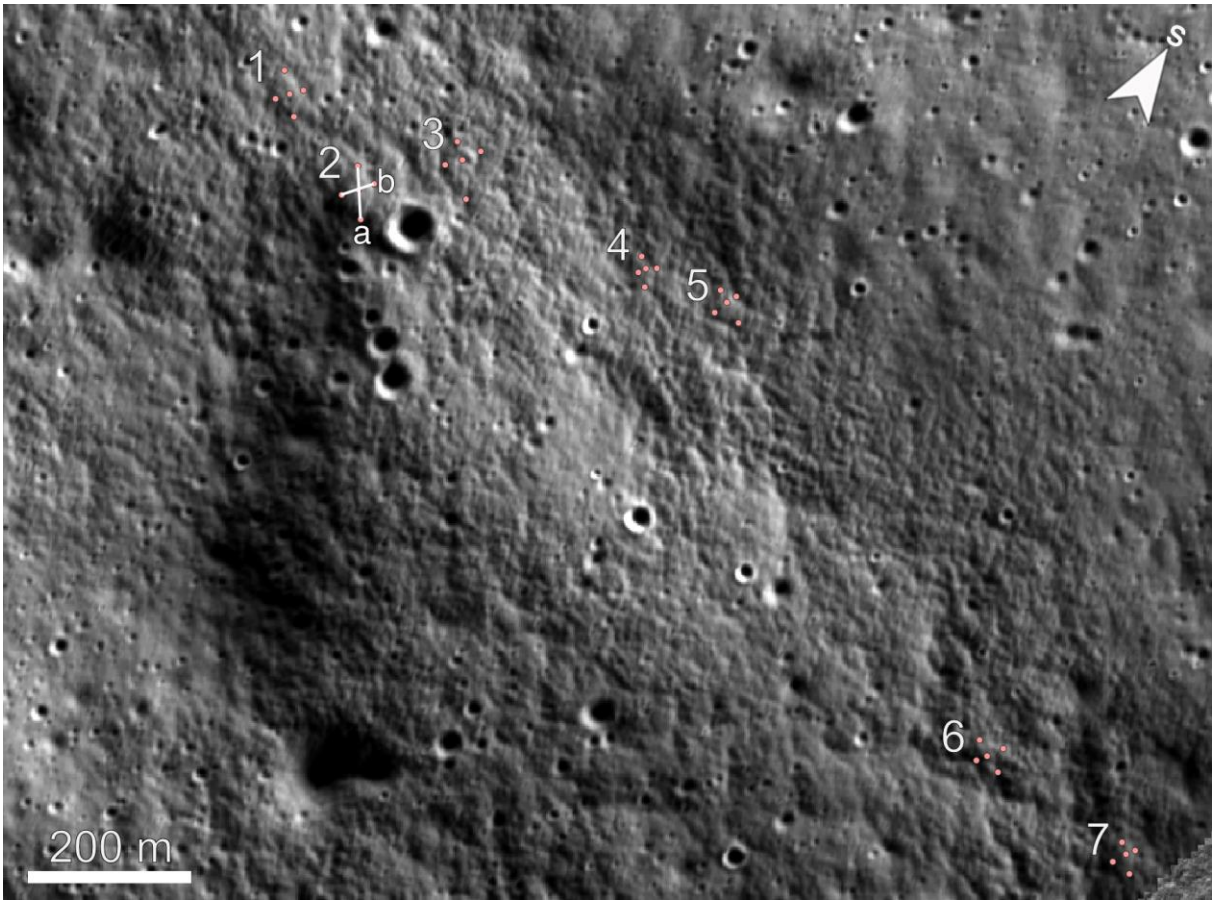

Fig. S1. Location (x, y) and elevation (z) data (pink dots) collected at the base and summit of EHT segments (Section 3.4.1). We calculated the distance between the points to estimate length (a), width (b), and lower-limit thickness of each numbered segment (Table S2).

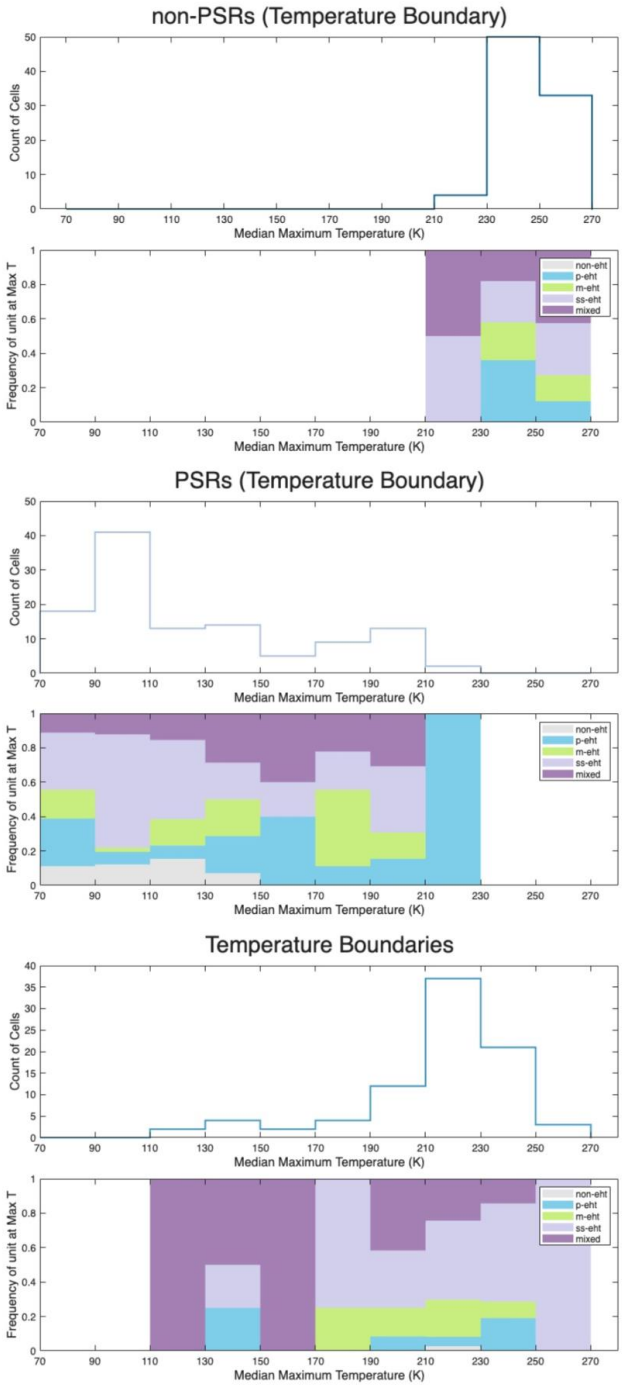

Fig. S2. Median maximum temperature where EHTs (p-eht, m-eht, ss-eht) are present or absent (unit non-eht) along selected non-PSR to PSR temperature boundaries (90° to 200° change in temperature) (Fig. 2; Section 2.1). Regions of interest mapped with 1 km by 1 km cells (1:20,000). EHT units have a similar frequency of occurrence at a given median maximum temperature across PSR to non-PSR boundaries. This indicates that variations in segment width (p-eht vs. m-eht) are not correlated with temperature changes.

Table S1. ShadowCam images used to map EHT in this study. Images used to measure EHT segments in Sverdrup crater are indicated by (*).

Image Name	Center Latitude	Center Longitude	Subsolar Azimuth	Subsolar Latitude	Phase Angle	Sun Direction
M044649276S	-89.815	312.716	210.4	-1.55	88.3	w
M044719990S	-89.738	247.575	209.5	-1.54	88.2	e
M043595815S	-89.513	75.279	223.4	-1.44	88.1	w
M016263567S	-89.495	299.367	354.2	-1.55	88.0	e
M043581673S	-89.489	80.309	223.6	-1.44	88.1	w
M043567531S	-89.452	85.137	223.8	-1.44	88.0	w
M013906270S	-89.428	294.089	202.0	-1.50	87.9	w
M042627229S	-89.305	228.999	234.2	-1.27	88.1	w
M015209918S	-89.218	66.104	187.0	-1.54	87.8	e
M015422102S	-89.214	326.218	184.5	-1.56	88.7	e
M013813510S	-89.131	334.489	203.2	-1.50	87.7	w
M013049982S	-89.112	22.788	212.6	-1.40	87.7	e
M013806376S	-89.082	336.115	203.3	-1.50	87.7	w
M017260683S	-89.073	179.143	342.4	-1.37	87.8	w
M046309302S	-88.936	55.718	188.5	-1.53	64.7	w
M046316326S	-88.934	55.786	190.9	-1.53	87.5	w
M016256498S	-88.917	308.739	354.2	-1.55	87.4	e
M046344504S	-88.909	57.587	190.5	-1.53	87.5	w
M013891999S	-88.893	308.092	202.2	-1.50	87.4	w
M045794708S	-88.892	138.168	197.4	-1.51	87.5	w
M046386768S	-88.891	61.709	189.9	-1.53	87.6	w
M046400856S	-88.846	62.117	189.7	-1.53	87.6	w
M047020718S	-88.840	274.810	2.4	-1.46	87.5	e
M045837135S	-88.836	122.432	196.9	-1.51	87.4	w
M015570616S	-88.828	36.566	182.6	-1.58	87.3	e
M015584760S	-88.819	35.389	182.4	-1.58	87.3	e
M014326049S	-88.797	214.638	196.9	-1.48	87.3	e
M046337483S	-88.782	55.529	188.2	-1.53	64.5	w
M046414944S	-88.774	61.569	189.5	-1.53	87.5	w
M014340196S	-88.769	215.158	196.7	-1.48	87.3	e
M015598905S	-88.764	35.002	182.1	-1.58	87.2	e
M047034860S	-88.762	271.882	2.2	-1.46	87.4	e
M014304831S	-88.752	216.251	197.1	-1.48	87.3	e
M045632103S	-88.737	186.455	199.1	-1.51	87.8	w
M014006185S	-88.736	268.751	200.7	-1.49	87.2	e
M045045299S	-88.721	237.533	205.8	-1.53	87.3	w

M015613050S	-88.720	34.429	181.9	-1.58	87.2	e
M046393836S	-88.708	58.374	187.6	-1.53	64.5	w
M014311905S	-88.705	217.481	197.0	-1.48	87.2	e
M042429241S	-88.699	265.991	236.5	-1.25	87.8	w
M014297760S	-88.696	218.043	197.2	-1.48	87.2	e
M014020459S	-88.696	265.427	200.5	-1.49	87.2	e
M014098966S	-88.687	247.548	199.5	-1.49	87.2	e
M014034733S	-88.666	262.178	200.3	-1.49	87.2	e
M046922042S	-88.663	335.883	183.8	-1.48	87.3	w
M014283615S	-88.657	219.574	197.3	-1.48	87.2	e
M014269469S	-88.657	219.955	197.5	-1.48	87.2	e
M045568487S	-88.655	193.114	199.8	-1.51	87.7	w
M046422010S	-88.646	58.904	187.3	-1.53	64.5	w
M014120377S	-88.642	243.403	199.3	-1.49	87.2	e
M017147552S	-88.635	185.974	344.0	-1.38	87.3	e
M014255322S	-88.634	221.211	197.7	-1.48	87.2	e
M015662557S	-88.631	35.021	181.2	-1.58	87.0	e
M014063281S	-88.631	256.435	200.0	-1.49	87.1	e
M045625061S	-88.627	184.710	194.7	-1.51	65.8	w
M045554349S	-88.625	193.912	200.0	-1.51	87.6	w
M045540210S	-88.621	195.214	200.2	-1.51	87.6	w
M014241176S	-88.614	223.002	197.8	-1.48	87.2	e
M014077555S	-88.605	254.231	199.8	-1.49	87.1	e
M015231137S	-88.601	83.459	186.8	-1.54	87.1	e
M017274822S	-88.599	170.320	342.2	-1.37	87.3	e
M015888812S	-88.581	20.783	358.4	-1.59	87.0	w
M014227032S	-88.580	226.081	198.0	-1.48	87.1	e
M015874671S	-88.551	23.918	358.6	-1.59	87.0	w
M045455390S	-88.535	204.004	196.5	-1.51	65.9	w
M046907958S	-88.522	338.170	183.9	-1.48	87.1	w
M017472794S	-88.513	119.484	340.2	-1.35	87.3	e
M013071410S	-88.513	48.476	212.3	-1.40	87.0	w
M045441249S	-88.512	206.450	196.6	-1.51	65.9	w
M015860531S	-88.511	26.891	358.7	-1.59	86.9	w
M045483651S	-88.500	198.902	201.0	-1.51	87.4	w
M013114234S	-88.497	46.617	211.8	-1.41	87.0	w
M015818113S	-88.495	33.673	359.2	-1.59	86.9	w
M013977670S	-88.492	281.515	201.1	-1.49	87.0	w
M017501083S	-88.485	110.586	339.9	-1.34	87.4	e
M013984807S	-88.468	279.737	201.0	-1.49	86.9	w
M015803975S	-88.460	34.485	359.4	-1.59	86.9	w

M013991944S	-88.445	278.005	200.9	-1.49	86.9	w
M014027624S	-88.442	268.430	200.4	-1.49	86.9	e
M014041898S	-88.423	265.281	200.3	-1.49	86.9	e
M013164210S	-88.414	44.600	211.1	-1.43	86.9	w
M015351409S	-88.402	63.487	185.4	-1.55	87.0	e
M015775698S	-88.398	35.359	359.7	-1.59	86.8	w
M045935905S	-88.396	98.999	195.8	-1.52	86.9	w
M046893874S	-88.391	340.076	184.1	-1.49	87.0	w
M046668500S	-88.388	19.277	186.8	-1.52	87.1	w
M046682587S	-88.387	17.650	186.6	-1.52	87.1	w
M045462442S	-88.369	200.044	201.3	-1.51	87.3	w
M014084720S	-88.368	257.660	199.7	-1.49	86.9	e
M046710760S	-88.365	14.118	186.4	-1.51	87.1	w
M015789838S	-88.364	34.502	359.6	-1.59	86.8	w
M046696674S	-88.363	15.660	186.5	-1.51	87.1	w
M017486942S	-88.357	115.776	340.1	-1.35	87.2	e
M045448301S	-88.344	202.258	201.5	-1.51	87.3	w
M017479869S	-88.341	118.053	340.2	-1.35	87.2	e
M044260468S	-88.317	24.067	214.9	-1.55	87.6	w
M043963567S	-88.307	92.223	229.5	-1.52	76.1	w
M046724847S	-88.301	11.439	186.3	-1.51	87.1	w
M017458650S	-88.300	124.829	340.4	-1.35	87.1	e
M014276541S	-88.298	227.696	197.4	-1.48	86.8	e
M046879789S	-88.294	342.186	184.3	-1.49	86.9	w
M045780579S	-88.281	138.484	197.5	-1.51	86.9	w
M047918593S	-88.280	170.224	351.8	-1.27	87.1	e
M045434161S	-88.278	204.245	201.7	-1.51	87.2	w
M044599808S	-88.274	317.521	211.1	-1.55	87.1	w
M015400916S	-88.261	58.462	184.8	-1.56	86.8	e
M047975139S	-88.252	162.151	351.2	-1.26	87.0	e
M045766439S	-88.251	142.772	197.7	-1.51	86.9	w
M045773531S	-88.244	140.495	193.6	-1.51	64.8	w
M017571809S	-88.235	94.211	339.2	-1.34	87.3	e
M015238210S	-88.235	87.679	186.7	-1.54	86.7	e
M044585668S	-88.234	321.843	211.3	-1.55	87.1	w
M015379699S	-88.234	62.236	185.1	-1.56	86.8	e
M045420021S	-88.218	206.536	201.9	-1.51	87.2	w
M045752300S	-88.215	146.897	197.9	-1.51	87.0	w
M045949999S	-88.197	97.259	195.7	-1.52	86.7	w
M046865704S	-88.190	344.243	184.5	-1.49	86.8	w
M045731113S	-88.188	152.735	194.0	-1.51	65.0	w

M045716974S	-88.182	156.249	194.1	-1.51	65.0	w
M013142827S	-88.177	49.108	211.4	-1.42	86.7	w
M045759392S	-88.174	144.445	193.7	-1.51	64.8	w
M046020452S	-88.173	83.408	194.8	-1.52	86.7	w
M013178511S	-88.167	46.000	211.0	-1.43	86.8	w
M046119086S	-88.159	69.699	193.7	-1.53	86.6	w
M016235313S	-88.153	316.532	354.5	-1.55	86.6	e
M046851618S	-88.142	347.013	184.7	-1.49	86.8	w
M017494018S	-88.141	114.811	340.0	-1.34	87.0	e
M046781190S	-88.138	1.357	185.7	-1.50	86.9	w
M015386771S	-88.133	62.516	185.0	-1.56	86.7	e
M013157108S	-88.127	48.372	211.2	-1.42	86.6	w
M016228243S	-88.125	318.405	354.6	-1.55	86.6	e
M045589727S	-88.123	180.660	195.1	-1.51	65.3	w
M045724024S	-88.120	153.928	198.2	-1.51	86.9	w
M045709885S	-88.119	157.286	198.3	-1.51	87.0	w
M045738163S	-88.110	150.134	198.0	-1.51	86.9	w
M045695746S	-88.098	160.276	198.4	-1.51	87.0	w
M045688697S	-88.092	161.797	194.3	-1.51	65.0	w
M045681607S	-88.075	163.214	198.6	-1.51	87.0	w
M045667468S	-88.065	166.240	198.7	-1.51	87.0	w
M043037309S*	-88.055	208.348	230.1	-1.33	88.0	w
M016199960S	-88.048	324.894	355.0	-1.56	86.5	e
M016192888S	-88.045	326.450	355.1	-1.56	86.5	e
M013199918S	-88.010	45.064	210.7	-1.43	86.6	w
M014509902S	-87.987	214.988	195.2	-1.48	86.5	w
M014481615S	-87.986	215.220	195.5	-1.48	86.5	w
M013563807S	-87.974	8.322	205.9	-1.49	86.7	w
M047953961S	-87.972	164.214	353.4	-1.27	63.8	e
M047925689S	-87.955	168.045	353.6	-1.27	63.7	e
M049175435S	-87.949	338.290	342.5	-1.07	65.5	e
M017465721S	-87.939	123.545	340.3	-1.35	86.8	e
M017515238S	-87.923	110.177	339.8	-1.34	86.9	e
M017508166S	-87.923	112.003	339.8	-1.34	86.8	e
M048010507S	-87.921	154.219	352.9	-1.26	63.8	e
M047996371S	-87.900	156.938	353.0	-1.26	63.8	e
M015245298S	-87.847	90.211	186.7	-1.54	86.3	e
M049203656S	-87.832	332.191	342.2	-1.06	65.5	e
M015019010S	-87.819	144.798	189.2	-1.51	86.7	w
M046837551S	-87.811	346.713	184.9	-1.50	86.5	w
M049189547S	-87.808	335.053	342.3	-1.06	65.4	e

M015011940S	-87.786	146.247	189.2	-1.51	86.7	w
M046034551S	-87.744	83.177	194.7	-1.52	86.2	w
M017444512S	-87.731	129.778	340.5	-1.35	86.5	e
M017451583S	-87.725	127.835	340.4	-1.35	86.6	e
M044776602S	-87.722	275.633	208.8	-1.54	86.3	w
M049182469S	-87.719	336.194	337.2	-1.06	86.8	e
M044741269S	-87.712	281.898	202.6	-1.54	66.2	w
M013364041S	-87.670	34.151	208.3	-1.46	86.4	w
M046006371S	-87.669	87.624	195.0	-1.52	86.2	w
M036660344S	-87.664	269.702	303.8	0.38	88.8	e
M017020275S	-87.663	205.943	345.6	-1.40	86.3	e
M031986883S	-87.651	261.379	356.4	1.45	89.1	w
M017529388S	-87.626	108.137	339.6	-1.34	86.6	e
M017522316S	-87.623	109.798	339.7	-1.34	86.6	e
M017013206S*	-87.612	206.709	345.7	-1.40	86.2	e
M013371167S	-87.578	33.724	208.2	-1.47	86.4	w
M045596805S	-87.565	174.249	199.5	-1.51	86.6	w
M015266526S	-87.559	88.708	186.4	-1.54	86.0	e
M044486705S	-87.534	341.638	212.6	-1.55	86.8	w
M045964102S	-87.530	96.330	195.5	-1.52	86.1	w
M044472567S	-87.492	344.224	212.8	-1.55	86.8	w
M014333120S	-87.475	231.386	196.8	-1.48	85.9	w
M015294818S	-87.451	84.074	186.1	-1.55	85.9	e
M017536449S	-87.450	107.271	339.5	-1.34	86.5	e
M015202882S	-87.444	100.929	187.1	-1.53	85.9	e
M013713665S	-87.430	345.532	204.5	-1.50	86.2	w
M013192788S	-87.417	49.094	210.8	-1.43	86.1	w
M015089713S	-87.415	127.783	188.4	-1.52	85.9	w
M015096784S	-87.415	125.967	188.3	-1.52	85.9	w
M017762770S	-87.411	67.314	337.0	-1.33	86.7	e
M013378306S	-87.384	33.149	208.1	-1.47	86.2	w
M013349783S	-87.367	34.927	208.5	-1.46	86.1	w
M014566485S	-87.366	213.185	194.6	-1.49	86.0	w
M017557691S	-87.341	103.149	339.3	-1.34	86.4	e
M044479665S	-87.321	341.788	205.2	-1.55	67.1	w
M013592377S	-87.309	2.017	205.6	-1.49	86.1	w
M047671223S*	-87.285	206.831	356.2	-1.32	62.7	w
M013578106S	-87.269	4.358	205.8	-1.49	86.1	w
M013628051S	-87.244	356.559	205.3	-1.49	86.0	w
M044465528S	-87.241	344.096	205.4	-1.55	67.1	w
M045066541S	-87.220	236.783	205.6	-1.52	85.9	w

M047628816S*	-87.216	210.620	356.6	-1.33	62.5	e
M048286198S	-87.204	93.004	347.9	-1.21	86.3	e
M049154262S	-87.171	340.005	337.5	-1.07	86.2	e
M048328620S	-87.149	86.009	347.4	-1.21	86.3	e
M076056859S*	-87.134	202.804	211.0	-1.52	86.4	w
M014417981S	-87.089	223.488	196.0	-1.48	85.6	w
M016815246S	-87.066	220.101	347.7	-1.44	85.9	e
M014396766S	-86.998	226.388	196.2	-1.48	85.5	w
M073688240S	-86.983	203.086	239.0	-1.43	87.6	w
M016822289S*	-86.954	219.807	337.9	-1.43	108.7	e
M015881775S	-86.872	15.155	358.5	-1.59	85.3	w
M014679620S	-86.852	199.820	193.3	-1.49	85.5	w
M013178538S*	-86.847	52.810	211.0	-1.43	85.6	w
M014290686S	-86.835	238.811	197.3	-1.48	85.3	w
M013678004S	-86.830	349.440	204.9	-1.49	85.7	w
M014594778S	-86.820	210.388	194.3	-1.49	85.5	w
M013685139S	-86.819	348.479	204.8	-1.50	85.7	w
M015867635S	-86.818	17.772	358.6	-1.59	85.2	w
M014262395S	-86.813	241.966	197.6	-1.48	85.3	w
M014785689S	-86.805	180.295	192.0	-1.50	85.5	w
M014813975S	-86.803	176.136	191.6	-1.50	85.5	w
M048229645S	-86.759	105.358	348.5	-1.22	85.8	e
M014743261S	-86.729	187.634	192.6	-1.49	85.4	w
M014234104S	-86.728	246.006	197.9	-1.48	85.2	w
M015591874S	-86.725	46.977	182.3	-1.58	85.1	e
M014863474S	-86.722	169.276	190.9	-1.50	85.5	w
M013271277S	-86.720	41.490	209.6	-1.45	85.5	w
M014205813S	-86.711	250.597	198.3	-1.49	85.1	w
M015563587S	-86.686	50.841	182.7	-1.58	85.1	e
M015577731S	-86.683	48.969	182.5	-1.58	85.1	e
M015606019S	-86.670	45.232	182.0	-1.58	85.1	e
M015839359S	-86.629	22.372	359.0	-1.59	85.0	w
M013292694S	-86.617	39.678	209.3	-1.45	85.4	w
M049422388S	-86.616	282.938	334.0	-1.00	86.3	e
M074190246S	-86.606	110.238	220.7	-1.48	72.4	w
M014248253S	-86.602	244.586	197.8	-1.48	85.1	w
M014615994S	-86.585	207.974	194.1	-1.49	85.3	w
M014608923S*	-86.570	208.684	194.2	-1.49	85.2	w
M013306967S	-86.551	38.587	209.1	-1.46	85.4	w
M013299831S	-86.549	39.173	209.2	-1.45	85.4	w
M013257009S	-86.470	43.591	209.9	-1.45	85.3	w

M014368487S	-86.455	231.409	196.5	-1.48	84.9	w
M013078591S	-86.445	65.543	212.3	-1.40	85.2	w
M014219966S	-86.335	249.828	198.1	-1.49	84.8	w
M014318987S	-86.305	237.540	197.0	-1.48	84.8	w
M049401249S	-86.210	288.230	340.0	-1.00	65.0	e
M015549453S	-86.177	53.679	182.9	-1.57	84.6	e
M013185652S	-86.166	53.551	210.9	-1.43	85.0	w
M049415364S	-86.137	285.567	339.9	-1.00	65.0	e
M013649454S	-86.092	352.636	205.2	-1.49	85.0	w
M013064324S	-86.043	68.636	212.5	-1.40	84.9	w
M046943236S	-85.530	316.346	183.5	-1.48	84.1	w
M086369576S	49.687	235.981	268.6	1.08	89.3	w

Table S2. Length, width, and height (lower-limit thickness) measurements of surficial EHT on the mound of Sverdrup crater floor (Section 3.4.1). EHT segments were selected using a ShadowCam 6-meter/pixel DEM and images taken under varying secondary lighting conditions (Table S1). We selected EHT segments based on consistent segment orientation in the overlapping images and resolvable EHT-associated topography in the DEM. Segment IDs and point measurements are shown in Fig. S1. Note that estimates are subject to 1 to 2 meters of uncertainty.

	a		b	
Segment ID	Length (m)	Height (m)	Width (m)	Height (m)
1	59.7	0.5	36.7	0.6
2	67.3	1.0	43.2	0.9
3	73.4	2.7	47.9	1.9
4	38.7	3.8	23.8	2.6
5	47.0	0.6	34.0	1.2
6	46.7	1.8	37.0	0.5
7	40.9	1.5	31.6	1.0